POLITECNICO DI TORINO

Master's degree thesis
in BIOMEDICAL ENGINEERING

Pre-treatment mapping strategies to enhance real-time temperature reconstruction in microwave cancer hyperthermia

Politecnico di Torino

Advisor
Prof. Giuseppe Vecchi
Company supervisors:
Eng. Maryam Firuzalizadeh
Dr. Rossella Gaffoglio
Dr. Giorgio Giordanengo
Dr. Marco Righero

Candidate
Andrea Tartaglione

March 2025

Abstract

The present thesis focuses on the development of error reduction methods in simulation-guided hyperthermia (HT) treatments, in particular for head and neck (H&N) tumors. HT therapy has gained increasing attention in the medical field due to its role in enhancing conventional cancer treatments such as radiotherapy and chemotherapy. By elevating the temperature of tumor tissues to 40-44 °C using non-ionizing microwave radiation, it increases the sensitivity of cancer cells to radiation and improves drug delivery without introducing additional toxicity. The benefits of HT have been well demonstrated in various tumor sites, including the cervix, breast, head and neck, skin, bladder, and esophagus. For sub-superficial and deep-seated tumors, phased-array antenna systems optimize the Specific Absorption Rate (SAR) within the tumor target, while minimizing the risk of hotspots in healthy tissues. Following clinically prescribed hyperthermia treatment planning (HTP) guidelines, patient-specific numerical simulations and temperature monitoring systems play a crucial role in controlling active electronic systems that adjust antenna feedings during treatment sessions while simultaneously monitoring the achieved temperature in different regions. This research focuses in particular on exploring pre-processing strategies to improve real-time reconstruction of the patients temperature distribution from limited invasive measurements. Chapter 1 provides a comprehensive overview of hyperthermia, covering its historical background, biological effects, and the mathematical modeling of tissue heating, highlighting the limits of the Pennes bioheat equation and the uncertainties associated with tissue properties, which can significantly affect simulation outcomes. Chapter 2 delves into the challenges associated with current temperature monitoring techniques, such as the invasiveness of thermometry catheters. The chapter introduces the high-resolution virtual model used in this study and the concept of parameter space. The procedures for electromagnetic and thermal simulations are detailed, as well as the method used to predict the patient temperature distribution from limited measurement data, which is based on inversion algorithms. Chapter 3 investigates the integration of S-parameters (active reflection coefficients) into the reconstruction process to enhance the accuracy of the predictions. The impact of this approach in different scenarios is evaluated using three metrics: χ_{95} (minimum error threshold in 95% of the volume and in 95% of the tested cases), ΔT (median of the pointwise absolute difference between the reconstructed and actual temperature map) and ΔT_{50} (absolute difference between the reconstructed T_{50} in the tumor volume and the actual T_{50} in the tumor volume). Chapter 4 focuses on optimizing the exploration of the parameter space by initially employing Sobol sequences to ensure uniform coverage, followed by targeted refinement in specific regions. Three types of refinement were investigated: two aimed at reducing redundancy in the basis matrix and one targeting underrepresented regions associated with higher errors. This approach seeks to identify the most effective sampling strategies to minimize the magnitude and occurrence of errors in both tumors and healthy tissues. The results of this analysis were reported in terms of error percentiles, χ_{95}, ΔT_{50} and ΔT_{90}.

Contents

Introduction

Cancer and its treatment have been among the greatest challenges in medical science for centuries. Systematic treatment for cancer patients began in the latter half of the 19th century, initially focusing only on the surgical removal of tumors. In the early twentieth century, the foundation of modern oncology was established, as therapies were refined to include drugs and dietary interventions [1]. Today, oncology has become one of the most interdisciplinary fields of research, encompassing diverse areas such as biology, biophysics, biochemistry, genetics, environmental sciences, epidemiology, immunology, microbiology, pathology, physiology, pharmacology, psychology, and virology. Although modern oncologic treatments, such as chemotherapy and radiation therapy, are highly effective, they come with significant side effects and remarkable impairments in patient quality of life. To maximize tumor destruction, these therapies are often pushed to their toxicity limits, but even then the results are not always satisfactory: achieving the desired tumor eradication often requires higher doses than what the body can safely tolerate. In the case of H&N cancer, even good clinical results after multimodal treatment (surgery plus chemoradiation) are accompanied by substantial side effects, often compromising social contacts with the patient and thus decreasing quality of life [2]. In search of alternative or complementary treatments that could minimize radiotoxicity, hyperthermia (HT) emerged as a promising method. Supported by numerous in vitro and in vivo studies during the latter half of the twentieth century and many phase III clinical trials in the last years, HT has demonstrated potential across a wide range of tumor sites [3–5], as explained in the first chapter.

This thesis is part of a broader effort to improve temperature reconstruction in microwave HT for the treatment of head and neck cancer. One of the biggest challenges in HT is accurately estimating the temperature distribution within the treated area, since inaccuracies can lead to suboptimal therapy outcomes or excessive heating of healthy tissues. This study focuses on refining pre-treatment strategies to enhance real-time temperature mapping using a limited number of invasive measurements. To address this, numerical simulations are used to model how different tissue properties influence the temperature distribution. Advanced reconstruction methods, based on inversion algorithms, are then applied to improve the accuracy of the estimation. The study investigates whether the integration of active reflection coefficients (S-parameters) or different parameter sampling strategies into the reconstruction process can improve predictions. By optimizing these aspects, this research aims to contribute to safer and more effective hyperthermia treatments.

Chapter 1

Hyperthermia: state of the art

1.1 Hypertermia definition

Heat therapy can be considered a traditional healing method. Even the first known, more than 5000 years old, written medical report from ancient Egypt mentions hyperthermia. The use of hyperthermia for cancer therapy was first documented by Hypocrites for the treatment of breast tumor. His approach was mainly supported by Greek philosophy, where fire (heat) had the highest level of abilities and freedom [1]. Several reports of tumor regression following high fever, secondary to bacterial infections such as erysipelas, were available in the nineteenth century. However, with the discovery of penicillin in the 1930s, as high fever secondary to these infections became rare, the phenomenon of tumor regressions after high fever was also rarely reported [3]. In modern times, hyperthermia therapy is defined as:

> "A type of treatment in which body tissue is exposed to high temperatures to damage and kill cancer cells or to make cancer cells more sensitive to the effects of radiation and certain anticancer drugs."[1]

HT exerts its therapeutic effects without chemical toxicity or the risks associated with ionizing radiation, as it is delivered through non-ionizing electromagnetic waves or ultrasound. This makes it a relatively safe treatment modality, with mild side effects primarily related to heating sensitive healthy tissues. In terms of temperature, the objective of HT is to warm the tumor region to approximately 43 °C, while keeping the heat in the surrounding healthy tissues in a tolerable range

[1] National Cancer Institute

and avoiding the presence of hotspots; however, in most clinical treatments, the achieved temperature range is 39 °C to 42 °C [6]. There are internal (interstitial or intraluminal) and external heating methods. External heating methods [7] are often characterized as:

1. **Whole body**: very high frequencies (200-375 MHz) and long application times (>2h) to reach 40.5 °C at most.

2. **Superficial**: frequencies in the range 400-1000 MHz in order to provide localized heating of skin and superficial tissues. The applicator is placed directly on the surface to be treated.

3. **Deep** : different frequency ranges (Regional:<100 MHz, Loco-regional: 100-300 MHz, Local: 300-1000 MHz) to heat larger and deeper regions of the body. In HT of tumors located beyond 2 cm from the skin, the temperature goal is often better achieved with a phased array approach, where an array of antennas is placed around the patient. The antennas are then suitably fed in amplitude and phase to create constructive wave interference to selectively heat the target region. For all electromagnetic (EM) waves, a circumferential array is the optimum arrangement since this maximizes the interference of the transverse waves, i.e. with the electric field component of the EM wave oriented along the patient-axis.

Many techniques involve, in conjunction with the applicator, a water bolus that works as a cooling system (useful to avoid hot spots on the patient's skin and healthy tissues) and to better couple the electromagnetic field radiated by the antennas into the body. Generally, HT is applied for 60 min before / after radiation therapy within a window of 0.5-4 hours, while with chemotherapy, HT is applied simultaneously or shortly after the chemoterapic regimen [7]. Hyperthermia has also been shown to be promising as a complement to proton beam radiotherapy (PBRT), leading to a greater reduction in tumor dimensions and sensitizing hypoxic radioresistant cells for more effective PBRT [6].

The addition of HT to radiotherapy (RT) and chemotherapy (CT) has demonstrated significant benefits in various tumor sites, such as breast, cervix, head, neck, rectum, bladder, esophagus, cutaneous melanoma, glioblastoma multiforme and choroidal melanomas. These benefits were measured in terms of improved complete response (CR) rates, prolonged time to progression (TTP) and enhanced quality of life (QoL) [8–10] . For example, in Table 1.1, a comparison of CR obtained with RT versus RT + HT is shown.

Site	Treatment	CR/Total	CR (%)	Odds Ratio (95% CI, p-value)
Breast	RT	88/181	48.6%	2.10 (1.34–3.30, 0.001)
	RT + HT	122/198	61.6%	
Cervix	RT	173/263	65.7%	2.19 (1.45–3.32, <0.001)
	RT + HT	200/251	79.6%	
Head & Neck	RT	183/364	50.3%	3.71 (2.55–5.38, <0.001)
	RT + HT	266/353	75.3%	
Rectum	RT	16/205	7.8%	2.15 (1.10–4.20, 0.025)
	RT + HT	36/208	17.3%	
Urinary Bladder	RT	35/86	40.6%	2.40 (1.25–4.62, 0.009)
	RT + HT	69/118	58.4%	
Esophagus	RT	24/132	18.2%	2.64 (1.34–5.20, 0.005)
	RT + HT	47/162	29.0%	
Lung	RT	2/70	2.8%	2.69 (0.51–14.22, 0.243)
	RT + HT	7/59	11.8%	

Table 1.1: Comparison of radiotherapy (RT) vs. RT + Hyperthermia (HT) applied in various tumor sites [10].

1.2 Biological effects of HT

Hyperthermia is used primarily in conjunction with radiation therapy and chemotherapy due to its thermobiological and immunological effects on the tumor environment [10], which can be summarized as:

- Increased sensitivity to chemoterapic drugs of hypoxic, nutritionally deficient cells in low pH;
- Inhibition of radiation induced DNA damage repair and increase in tumor DNA damage;
- Sensitization of the S phase cells [2];
- Local modification of the phenotype of the tumor cells and their micro-environment which might render the tumor immunogenic (i.e. cause the body to make an

[2]S phase is the period of DNA synthesis during which the cell replicates its genetic content, occurring between G1 phase and G2 phase.

immune response against it).

- Direct activation of immune cells present in the tumor and its microenvironment, reflecting an "in situ tumor vaccination" (Figure 1.1).

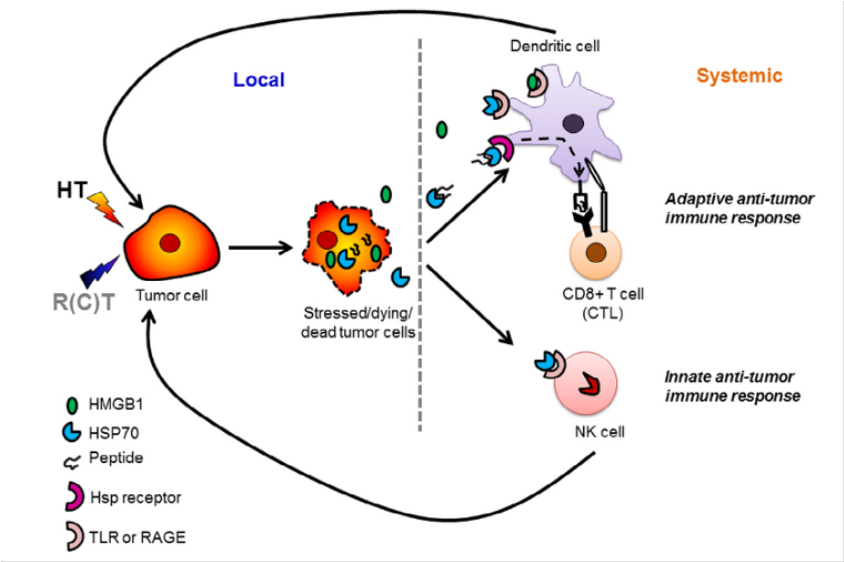

Figure 1.1: **In-situ vaccine mechanism:** Heated tumor cells release heat shock proteins (e.g., HSP70) and danger signals like HMGB1. HSP70 transports tumor peptides to dendritic cells (DCs) via HSP receptors. DCs process and present these antigens through MHC class I molecules to CD8 cytotoxic T lymphocytes (CTLs) with necessary co-stimulation. HMGB1 binds to DCs via toll-like receptors (TLRs) or RAGE, enhancing antigen cross-presentation. Additionally, danger signals activate natural killer (NK) cells, which, together with CTLs, lyse the tumor cells. From [10].

The vessels in the tumor are generally leakier and have a more chaotic structure compared to healthy tissues. This causes less nutrient diffusion and makes them unable to remove heat efficiently, which can lead to higher temperatures during heating, independently of any type of focusing. That is why, in easy-to-heat tumors and / or in the hypoxic part of the tumor, treatment reaches temperatures equal to or greater than 43 °C (always complying with safety requirements) resulting in direct death of the malignant cells. Direct damage at lower temperature is also typical in some types of tumor that have a higher intrinsic sensitivity to hyperthermia (e.g., sarcomas, melanomas) [11]. In summary, during hyperthermia treatments, the heat generated induces biological damage due to the inability of the tissue to dissipate excess energy at the same time it is supplied. The mass-normalized rate of energy absorption by a biological body following hyperthermia is estimated by one of the most important parameters used in radioprotection and in the clinical applications of electromagnetic fields: the Specific Absorption Rate

(SAR).

1.3 Mathematical model

At frequencies above 100 MHz, heating is generated mainly by mechanical friction between adjacent polar water molecules (oscillations at more than 100 million cycles per second) [12]. In general, for a volume Ω without internal sources, the energy balance is [13]:

$$p_{\text{diss},\Omega}(t) + \frac{dW_\Omega(t)}{dt} = p_{\delta\Omega}(t) \tag{1.1}$$

where $p_{\text{diss},\Omega}$ [W] is the power dissipated in the volume, W_Ω [J] is the stored energy in Ω, and $p_{\delta\Omega}$ [W] is the energy transport through the surface of Ω. The dissipated power in function of the volume is defined as:

$$p_{diss,\Omega}(t) := \lim_{\Delta t \to 0} \frac{\Delta W}{\Delta t \, d\Omega} \tag{1.2}$$

where W is the work of the electromagnetic field, defined as the product of the electromagnetic force on the free charges and their displacement $\underline{s}$:

$$W = (F_{Coulomb} + F_{Lorentz}) \cdot \underline{s} = q \, (\underline{\mathscr{E}} + \underline{v} \times \underline{\mathscr{B}}) \cdot \underline{v} \, t = \rho \, \Omega \, (\underline{\mathscr{E}} \cdot \underline{v}) \, t \tag{1.3}$$

with $\underline{\mathscr{E}}$ being the electric field, $\underline{\mathscr{B}}$ being the magnetic flux density and ρ being the charge volumetric density. At this scale, the current $\underline{\mathscr{J}}$ can be approximated equal to the conduction current:

$$\underline{\mathscr{J}} = \rho \underline{v} \Rightarrow W = (\underline{\mathscr{E}} \cdot \underline{\mathscr{J}}) \, \Omega \, t \tag{1.4}$$

Consequently, considering Equation 1.2 and that the conduction current in a simple mean can be also be written as $\underline{\mathscr{J}} = \sigma \underline{\mathscr{E}}$ (Ohm law for a simple mean [3]), the dissipated power is:

$$p_{diss,\Omega}(t) = \underline{\mathscr{E}}(t) \cdot \underline{\mathscr{J}}(t) = \sigma |\underline{\mathscr{E}}(t)|^2 \tag{1.5}$$

The heat generated by the electromagnetic field in the i-th tissue can be calculated as the time average of the power dissipated in the tissue itself [14]:

$$q_{\text{EM}} := \frac{1}{T} \int_0^T \frac{p_{\text{diss},\Omega}(t)}{d\Omega} dt \tag{1.6}$$

By merging 1.5 and 1.6 , we have:

$$q_{EM} = \int_0^T \sigma |\underline{\mathscr{E}}(t)|^2 \, dt \tag{1.7}$$

[3] Paul Drude model

where T is the thermal diffusion time scale. The effective electrical conductivity σ (S/m) is a parameter that accounts for all electrical losses in the material due to currents driven by the EM field. In the case where the frequency of the field used is "fixed", it is more convenient to write q_{EM} in its time-harmonic form; thus:

$$q_{\text{EM}} = \sigma |\underline{E}(P)|^2 \tag{1.8}$$

When Equation 1.8 is normalized by the tissue density (ρ), it is referred to as the SAR $[Wkg^{-1}]$ and corresponds to the rate of EM energy absorption per unit weight of tissue:

$$\text{SAR} = \frac{\sigma |E|^2}{2\rho} \tag{1.9}$$

1.3.1 Pennes bio-heat model

During the treatment planning phase, heat transport in the human body is typically modeled using the *Pennes Bioheat Transfer Equation* (PBHE) [15]:

$$\rho C \frac{\partial T}{\partial t} = k\nabla^2 T + q_s \tag{1.10}$$

where, for each considered tissue, ρ is the tissue mass density [kg m^{-3}], C is the heat capacity [J kg^{-1}K^{-1}], k is the thermal conductivity [W m^{-1}K^{-1}], and q_s [W m^{-3}] is the source term. The source term can be expressed as $q_s = q_{\text{hs}} + q_m + q_p$, where:

- q_{hs}: the heat source term, which is the $\mathbf{q}_{\text{EM}}$ obtained in 1.8 :

$$q_{\text{hs}} = q_{\text{EM}} = \sigma |\mathbf{E}(P)|^2 \tag{1.11}$$

- q_m: the metabolic heat generation term (heat produced by metabolic reactions)
- q_p: the heat loss due to blood perfusion which can be expressed as:

$$q_p = -\omega_{\text{bl}} C_{\text{bl}} \rho_{\text{bl}} (T - T_{\text{bl}}) \tag{1.12}$$

  where ω_{bl} is the blood perfusion rate [ml kg^{-1}K^{-1}], C_{bl} is the specific heat of blood [J kg^{-1}K^{-1}], ρ_{bl} is the blood mass density, and T_{bl} is the arterial blood temperature [K]. The negative sign reflects the compensatory role of blood: when the temperature of the tissue increases, blood removes heat; when the temperature of the tissue falls, blood delivers heat. The limitations of this model will be discussed in Section 1.3.2.

In general, the metabolic heat generation term is considered negligible ($q_m \approx 0$) to simplify the problem. In the instant following the irradiation, blood transfer from the arteries, thermal conductivity and convection can be neglected. Thus,

at $t = 0^+$, assuming the heat source remains constant over time, equation 1.10 becomes:

$$\rho C \frac{\partial T_{in}}{\partial t} = q_{\text{hs}} = \sigma |\mathbf{E}(P)|^2 \tag{1.13}$$

Considering 1.9, the result is:

$$\text{SAR} = C \frac{\partial T}{\partial t} \tag{1.14}$$

Equation 1.14 highlights the relationship between SAR and the initial increase in temperature. For example, to raise the temperature of muscle tissue by 1°C in 1 minute, an average SAR of 60 W/kg is required.

1.3.2 Uncertainty of Tissue Properties

The PBHE provides a simple way to model the behavior of the biological system, but it has limitations. First, it has been shown to be valid only for a large region of tissue with healthy microvasculature and blood flowing through vessels with isotropically distributed orientations. For a more accurate modeling of the impact of blood vessels with diameter greater than 0.2 mm on the local tissue temperature, the *Discrete Vasculature (DIVA) models* [16] have been developed. These models require the geometry of the vascular tree along with information on the diameters and flow rates in the various sections of the vascular tree and as a result it is unable to produce temperature predictions within a clinically realistic time frame. Unfortunately, regardless of how accurately the blood vessel tree is modeled prior to heating, static PBHE and DIVA models are only approximate, since blood vessel size and perfusion rates change dramatically as a function of temperature and duration of heating [17].

Second, the thermal and dielectric properties are tissue-dependent, frequency-dependent, temperature-dependent and exhibit variability across patients. Gabriel et al. originally measured and tabulated normal human dielectric properties [18]. A more comprehensive database, including thermal and physiological properties, is available in the IT'IS Tissue Properties Database [19], which also provides statistical information on the spread and standard deviation per tissue for the different parameters. The limits of this database will be discussed in Section 1.3.2.

Third, obtaining new accurate tissue properties is very challenging; for example, ex vivo dielectric measurements with an open-ended coaxial probe are prone to inaccuracies due to tissue degradation, fluid loss, and the difficulty of achieving proper probe contact and pressure [4]. The dielectric properties are also sensitive

[4]Despite its limitations, the open-ended coaxial probe remains widely used due to its ability to perform broadband, non-destructive measurements across frequency ranges, its suitability for in vivo applications with bio-compatible probes.

to temperature changes and thus strict environmental control is needed during testing. In vivo measurements face further complications, such as the heterogeneity of living tissues, physiological variability (e.g., hydration and blood perfusion), motion artifacts caused by respiration or movement, and unstable probe-tissue interface on irregular or moving surfaces. Finally, ethical and safety considerations limit the experimental conditions [20].

This variability in dielectric and thermal properties can contribute to an approximately 20% inaccuracy in both SAR and temperature predictions (as stated by [21], but also shown in this thesis), highlighting the need for a cautious and precise approach, particularly in the head and neck region, where excessive heating could lead to significant and potentially irreversible damage due to the presence of thermosensitive tissues (e.g., cerebrum, cerebellum, brain stem, and spinal cord).

1.4 HT treatment plan for H&N cancer

SAR and temperature distributions in the clinical target volume[5] (CTV) and in the healthy volume strongly correlate with the clinical outcome [22]. As mentioned above, when tumors are located beyond 2 cm from the skin, heating is better achieved with a phased array of antennas; such applicators cannot be controlled intuitively while doing the HT treatment (i.e. following the historically applied subjective steering based on empirical knowledge and patient complaints).

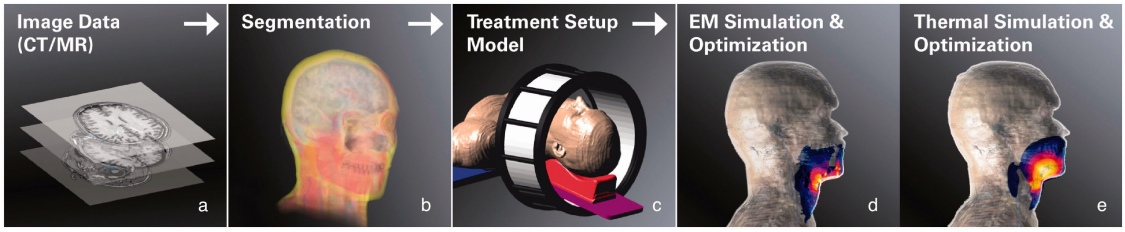

Figure 1.2: Schematic view of hyperthermia treatment plan [23]

Rather, a more objective-based patient-dedicated treatment plan is followed, as described in [3]:

1. *Image acquisition and modeling*: CT or MRI images are acquired with the patient in treatment position. A 3D patient model is created via manual, semi-automatic, or automatic segmentation of different tissue types (Figure 1.2, a and b). The position of the patient model relative to the applicator must be documented and reproduced during the actual treatment.

[5]Tissue volume that contains the gross tumor volume (GTV) and subclinical microscopic malignant lesions

2. *Virtual insertion into software*: The segmented patient model and a 3D model of the applicator are inserted into an electromagnetic simulation software based on Finite Elements (FE) or Finite-Difference Time Domain (FDTD) methods. Tissue-specific electromagnetic (*relative permittivity* ε_r [−], *electric conductivity* σ [S m^{-1}]) and thermal parameters (*thermal conductivity* k [W $m^{-1}K^{-1}$], *perfusion* w [ml $kg^{-1}K^{-1}$]) are assigned, usually using the baseline values in the IT'IS database. This digital twin is used for the applicator configuration and to explore possible temperature distribution scenarios.

3. *Applicator configuration*: The phase(s), amplitude(s) and frequency(ies) of the applicator (steering parameters) are optimized to concentrate heat on the tumor while avoiding overheating surrounding healthy tissues (Figure 1.2, c and d). Various optimization strategies have been developed for phased array systems, which can be subdivided into temperature-based and SAR-based optimization methods. The former focuses on maximizing tumor temperatures while maintaining hard or soft constraints (penalty terms added to the objective function) on healthy tissues. Temperature-based optimization methods are usually based on Pennes model or DIVA model, but solving the corresponding differential equation is extremely computationally intensive. SAR-based optimization aims to maximize the ratio of absorbed power in the tumor versus surrounding areas. This method can predict hotspots in a faster and not necessarily less accurate way with respect to the temperature-based one, as it accounts only for the electric field and is not influenced by the choice of the thermal model and their related inaccuracies. A more detailed description of the two techniques can be found in [24].

4. *Placement of thermometry catheters:* Closed-tip thermometry catheters are placed interstitially, intraluminally, and/or on the skin. A CT scan is performed to accurately document the catheter tracks.

5. *Patient positioning:* In the hyperthermia treatment room, the patient is positioned relative to the microwave applicator according to the optimized setup.

6. *Insertion of thermometry fibers and probes:* Optical thermometry fibers are inserted into the interstitial and intraluminal catheters. Additional thermometry probes are placed on the skin and at the inflow and outflow of the water bolus.

7. *Waterbolus preparation:* The water bolus is filled with demineralized water circulated at a temperature range of 20-30 °C. It improves the coupling between the electromagnetic field and the patient and to controls skin surface temperature, avoiding superficial hotspots.

8. *Transfer of Optimized Parameters:* The optimized phase and amplitude settings are transferred to the hyperthermia system unit and applied during the

treatment session (Figure 1.2, e). Power is increased incrementally (one step per minute).

9. *Temperature monitoring and safety measures*: Radiation is stopped if temperature probes indicate tolerance limits are exceeded or if the patient reports pain. Many quantitative assessments can also be used as stopping criteria, for instance the *maximum input RF power* defined by [22] as the power that leads to a threshold SAR of 60 Wkg^{-1}, averaged over cubic spaces of 1 cm^3, in the spinal cord. If a hot spot is detected, amplitude and phase coefficients are re-optimized.

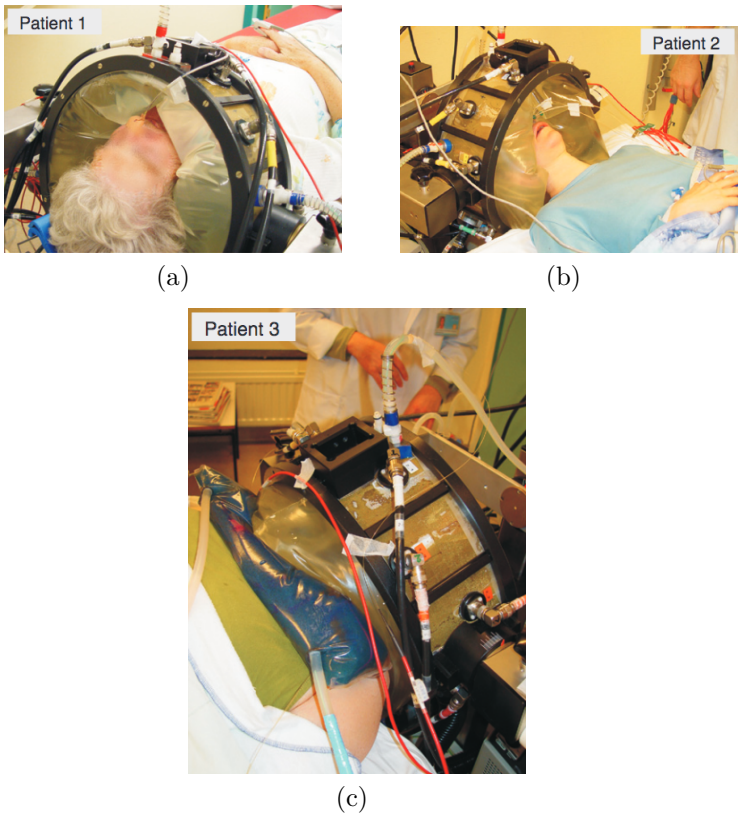

(a) (b)

(c)

Figure 1.3: Pictures of the setups for three different patients discussed in [25], with tumors in the oropharynx (a), nasopharynx/nasal cavity (b) and thyroid (c), respectively.

Three examples of complete patient setup are given in Figure 1.3.

Chapter 2

Experimental setup

2.1 Critical aspects of temperature monitoring

Current MW hyperthermia treatments for deep tumors are driven by qualitative patient complaints, where heating is steered from a region of complaint by adding constraint factors for that region, and temperature monitoring with a few measurement points [7]. As mentioned in Section 1.4, the most common approach involves inserting invasive interstitial and intraluminal catheters containing probes into the CTV. The probes often consist of fiber optic sensors (FOSs) that do not interfere with the electromagnetic field. However, this practice poses significant challenges for patients. The placement of catheters can cause serious morbidities, including pain, local inflammation, and other side effects [22]. In addition, temperature probes provide limited spatial information, as they measure only along the catheters insertion path. Magnetic resonance thermometry (MRT) and computer simulations are the two non invasive or minimally invasive alternatives [7] that are being developed.

MRT provides 3D temperature maps superimposed with the patient anatomy using the proton resonance frequency shift method [26], allowing operators to obtain MRT maps about every 10 or 15 min and only now are starting to be used in HT treatment guidance. Magnetic resonance imaging can also be used to measure perfusion, with higher accuracy, using a variety of techniques [27]. Unfortunately, its widespread use is hindered by the high operating costs of MR scanners and the adaptations of the heating equipment to magnetic fields (they mainly consist of metallic structures). Currently, it is also not feasible for moving tumors (abdomen) and it is difficult to maintain stable temperature measurements over long durations 6090 min due to motion artifacts (respiratory motion, organ motion and air travel) and magnetic field drift artifacts [7, 24].

Computer simulations are typically used to generate a pre-treatment plan, but the same tools are also used for online treatment guidance, which uses a feedback scheme that is updated in real-time to optimize the treatment delivery. They use numerical methods, measured temperatures and the 3D patient-specific anatomical model to generate SAR and temperature maps of the region of interest (ROI).

This research is focused on computer simulations. Reconstructing large temperature maps from few and possibly noisy measurements is an "ill-posed problem", meaning that small variations in the input data can lead to large variations in the output. Moreover, their accuracy is highly dependent on the dielectric and thermal properties of tissues, which are not measured in the specific patient. This often leads to unacceptable reconstruction errors that can negatively impact the outcome of therapy. To investigate preprocessing strategies aimed at improving the prediction of patient temperature distribution, a controlled and realistic experimental setup was required. In this chapter, this setup is described, as well as the mathematical framework used to address the ill-posed nature of the problem, and some concepts that will be used in Chapter 3 and Chapter 4.

2.2 Virtual model

Considering the HTP guidelines mentioned in Section 1.4 and to reproduce realistic treatment conditions, one of the human models present in the Virtual Population (ViP) of the Sim4Life software (see Appendix A) was chosen. The ViP models represent a series of comprehensive high-resolution anatomical digital twins generated from magnetic resonance imaging data of volunteers. These models are used for biophysical and biomedical modeling and simulations, such as evaluating the safety of medical implants and characterizing specific demographic groups. Specifically, the experiments presented in this thesis were performed using Yoon-Sun (2.1b), whose characteristics are detailed in Table 2.1c. To simulate an applicator, a circular array of 8 probe-fed patch antennas was designed in Sim4Life, with features optimized to obtain a working frequency of 434 MHz. These components, together with the water bolus, were then integrated into the ViP model, as shown in Figure 2.1a.

A tumor (volume 4041.44 mm^3 and overall dimensions 18.07 mm, 16.26 mm and 26.25 mm along the x, y, z axes, respectively) was modeled inside the phantom neck region (Figure 2.2), to create a target region and simulate a realistic HT treatment plan.

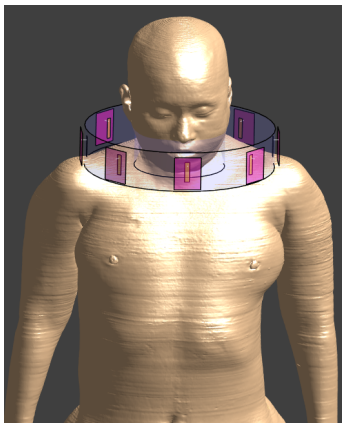

(a)

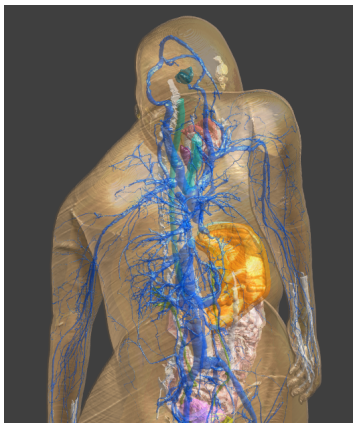

(b)

Characteristic	Value
Age	26 [year]
Height	1.52 [m]
Weight	54.6 [kg]
BMI	23.6 [kg m^{-2}]

(c)

Figure 2.1: Yoon Sun ViP model characteristics and visualization in Sim4Life: (a) External view with antenna system and water bolus, (b) with visible internal tissues, (c) key phantom characteristics.

Later, the entire volume was divided into a finite number of cubic elements (voxels) with the *Voxeler* settings within the S4L workspace. Given the trade-off between computational efficiency and model accuracy, the phantom was discretized using a 2 mm maximum voxel size, with finer resolutions (1 mm) applied to the neck region and an even more detailed, automatic refinement within the tumor volume. This multiresolution approach ensures high fidelity in critical regions while maintaining feasible computation times for iterative simulations [1]. Each voxel is treated as a Yee cell, and the finite-difference time-domain method (FDTD) is applied (see Appendix A), allowing for the electric and magnetic fields to be evaluated pointwise for a given excitation of the antennas.

[1]From S4L manual: "[...]in an evenly spaced mesh, if the mesh step size is halved, the storage needed increases eightfold, and the computation time becomes 16 times longer."

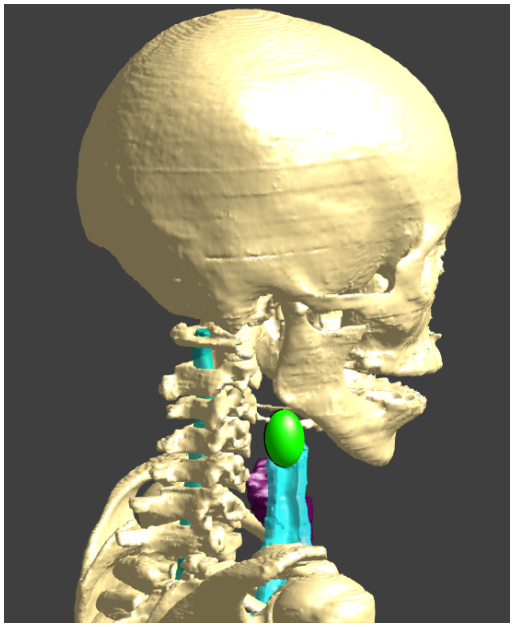

(a) Posterior-lateral view of the tumor (ellipsoid in green), together with the trachea (light blue), the spinal cord (aquamarine) and the thyroid glands (purple)

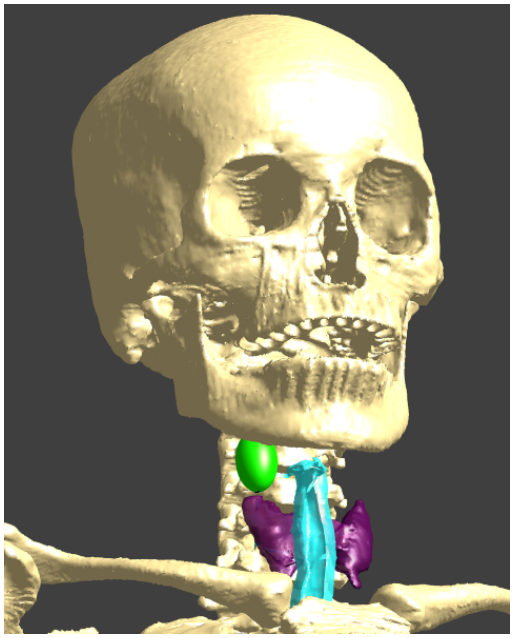

(b) Fronto-lateral view of the tumor (ellipsoid in green), together with the trachea (light blue), the spinal cord (aquamarine) and the thyroid glands (purple)

2.3 Antenna feedings optimization

Once the ROI has been voxeled, the next step consists in optimizing the amplitudes and phases of antennas with SAR, in particular using a Particle Swarm Optimization (PSO), which is a computational method inspired by the social behavior of birds and fish that is commonly used for complex systems. It works by simulating a "swarm" of particles (potential solutions) that move through the solution space [28]. Each particle adjusts its position based on the following:

- *Personal best position* (pBest): the best solution the particle has achieved so far.
- *Global best position* (gBest): the best solution found by the entire swarm.
- *Velocity*: a vector determining the direction and magnitude of the particle's movement, influenced by the two bests above.

An *EM FDTD Multiport Simulation* conducted in Sim4Life was used to solve Maxwell's equations by activating one antenna at a time with a normalized power input of 1 W. Under these conditions, the total electric field would naturally superimpose at the geometric center of the array, failing to target the tumor due to the

absence of phase and amplitude diversity. To address this, the individual electric fields generated by each antenna and computed for each voxel were exported to MATLAB, where the PSO algorithm was applied to determine the optimal set of feeding coefficients. The total electric field E can be expressed as:

$$E = \sum_{n=1}^{N} \tilde{\nu}_n \cdot E_n \tag{2.1}$$

In this expression, E_n represents the electric field produced by the n-th antenna when it operates independently (i.e., all other antennas are deactivated) and $\tilde{\nu}_n$ are the coefficients that need to be optimized. For the optimization of both phase and amplitude, $\tilde{\nu}_n$ can be written as:

$$\tilde{\nu}_n = C \cdot \nu_0 \cdot \zeta_n \cdot e^{i\phi_n} \tag{2.2}$$

where ϕ_n are the phases of the antennas included in the range $[0, 2\pi]$, $\nu_0 = \sqrt{2R_0P_0}$ with $R_0 = 50\,\Omega$ and $P_0 = 20\,\mathrm{W}$, ζ_n is included in the range $[0, 1]$ and C is:

$$C = \frac{1}{\sqrt{\sum_n \zeta_n^2}} \tag{2.3}$$

The fitness function to minimize was the Hotspot to Tumor Quotient (HTQ), identified by Canter et al. [29] as particularly effective for SAR-based optimization. HTQ is defined as:

$$HTQ = \frac{\langle SAR_{V1} \rangle}{\langle SAR_{target} \rangle} \tag{2.4}$$

where $\langle SAR_{V1} \rangle$ denotes the average SAR within the top 1% of healthy tissue exhibiting the highest SAR values, and $\langle SAR_{target} \rangle$ represents the average SAR within the tumor volume. Minimizing HTQ promotes effective energy deposition within the tumor while reducing unwanted heating of healthy tissues. The results of the optimization are presented in Table2.1. In the experiments that will follow, these values will be used as feedings (phase and amplitude) for each antenna, respectively.

In a clinical setting, the power settings (P_0) should be adjusted to have sufficient heating of the target volume and to avoid hotspots. Here, the focus is on the accuracy of the temperature reconstruction rather than the closeness of the temperature to clinically effective values, so the input power is left untouched. An example of the SAR distribution with input power of 60 W is shown in Figure 2.2 in two planes that cut the tumor centroid; the tumor is shown as a green ellipsoid, with decreased opacity when necessary to highlight SAR focusing.

Table 2.1: Phase-amplitude optimization

Antenna (n.)	ϕ [deg]	ζ [V]
1	27.02	0.9281
2	32.51	0.8635
3	0	0.7359
4	0	0.1951
5	307.25	0.5934
6	293.51	0.6389
7	311.57	0.9966
8	0	0.8670

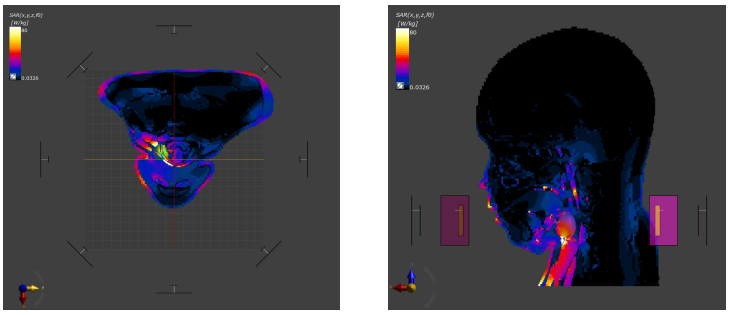

(a) (b)

Figure 2.2: Optimized SAR profiles obtained with the PSO algorithm, normalized at 60 W input power; XY (a) and XZ (b) slices corresponding to maximum SAR

2.4 EM and Thermal simulations

Once the feedings have been chosen and the volume has been voxeled, an EM *Array Simulation* is run in Sim4Life, exciting all the antennas simultaneously. The dielectric and thermal properties of each one of the tissues of the phantom are automatically assigned following the baseline values registered at the ITI'S foundation, but can be modified within the simulation settings. In Chapter 3, the study involved performing a series of simulations that varied both properties for muscle, fat, subcutaneous adipose tissue (SAT), skin and tumor tissues; in Chapter 4 , mainly due to time limitations, only different combinations of thermal parameters were considered in the four tissues. For each imposed set of properties ξ, the overall field is computed and the Power Loss density [Wm^{-3}] is extracted and saved in a specified folder as a cache file. Subsequently, it is used as source for a *Stationary Thermal Simulation* (TS), which assumes steady-state conditions where the temperature no longer changes with time, focusing on the final equilibrium distribution. In fact, the European Society of Hyperthermic Oncology (ESHO) guidelines [30] recommend only considering the steady-state version of PBHE due to its lower

computational time which is trivial for a real-time application. This is equivalent to solving the following equation for T:

$$k\nabla^2 T + \sigma|\mathbf{E}(P)|^2 - \omega_{\mathrm{bl}} C_{\mathrm{bl}} \rho_{\mathrm{bl}} (T - T_{\mathrm{bl}}) = 0 \tag{2.5}$$

Finally, as the thermal simulation is carried out, a temperature value is assigned to each voxel of the phantom, defining a temperature map uniquely related to a given set of tissue properties. The temperature map is then exported to Matlab, after a little pre-processing: a Sim4Life analysis tool called *mask filter* was used to mask out each antenna, the background, and the internal air, therefore considering only the voxels of the tumor and healthy tissues. Since the extracted file also includes the X, Y and Z coordinates of each voxel, only a certain interval of points have been selected in Matlab's workspace, in particular the one corresponding to Yoon Sun's neck area. The only thing needed is the index range of the desired slices, which in this case was 60 to 120. The resulting 3-dimensional map is reshaped into a $[n \times 1]$ vector, with n equal to the number of voxels in the region of interest, namely 374624, containing NaNs in the masked portions and point-wise temperature values (in °C) in the rest of the volume. It should be highlighted that, in this scenario, the tumor volume represents 0.16% of the total ROI.

2.5 Reconstruction method

The reconstruction method aims to estimate the temperature distribution of the entire ROI of the patient based on a limited set of invasive temperature measurements. This is an important requirement, as real-time knowledge of the temperature distribution is required to control the energy settings. However, directly measuring the entire temperature field in a clinical setting is challenging due to the invasive nature of thermometry catheters and the high cost of alternative imaging-based methods.

Let us assume that $m_b,\ b = 1, \ldots, B$ is a subset of unique combinations of parameters used in EM and thermal simulations: then it is possible to build B different temperature maps of elements n that represent possible outcomes of a simulation for the same patient and consequentially different possible adjustments to the initial treatment plan. These maps can be obtained in a pre-treatment phase. Let us also assume that $m_t,\ t = 1, \ldots, A$ is another subset of unique points in the parameters space, such as that:

$$\forall\, \boldsymbol{\psi} \in m_t, \quad \forall\, \boldsymbol{\xi} \in m_b, \quad \boldsymbol{\psi} \neq \boldsymbol{\xi}, \quad \text{with } m_t, m_b \subset \mathbb{R}^{16}$$

with ψ, ξ any given combination of the respective subset. The temperature maps generated with m_t can be used as *target maps*, i.e. a dataset of simulated temperature maps on which the reconstruction method can be tested and that ultimately form the matrix Φ_t. During treatment, the measured temperatures along

the catheter track provide a partial snapshot of the patients actual temperature map. The reconstruction method assumes that the true temperature distribution can be approximated as a linear combination of the precomputed maps with weighting coefficients β that are obtained solving the following equation:

$$\Phi_{|catheter\ points} \times \beta = f(\mathbf{r};\psi)_{|catheter\ points} \tag{2.6}$$

where

- $f_{|catheter\ points}$ represents the measured temperatures along the catheter track. In a clinical setting, the full temperature map f is unknown, making it impossible to directly assess the reconstruction error; however, in this experimental setup, one of the *target maps* previously defined is used as ground truth.
- $\Phi_{|catheter\ points}$ represents the temperatures at the same catheter points in the matrix Φ $[n \times B]$, where all pre-treatment simulated maps are stored.

Once the vector β $[B \times 1]$ is computed, it is possible to attempt reconstructing a $[n \times 1]$ approximation $\hat{f}$ of the unknown patient's map as follows:

$$\Phi_{|ROI} \times \beta = \hat{f}(\mathbf{r};\psi)_{|ROI} \tag{2.7}$$

Listing 2.1: Example of inversion with `lsqlin` function enforcing non-negativity and sum-to-one conditions

```
% bound ub is not neccessary
beta = lsqlin(Phi(ind_Cath,:), f(ind_Cath)+N,[],[],ones(1,B
    ),1,zeros(B,1),+inf,1);

f_hat = Phi(ind_ROI,:) * beta;
err = abs(f_hat - f(ind_ROI));
```

The reconstruction error therefore is:

$$err = |\hat{f}(\mathbf{r};\psi) - f(\mathbf{r};\psi)| \tag{2.8}$$

where $\mathbf{r} \in \Omega = ROI \subset \mathbb{R}^3$, and ψ is the parameter set of the target map. It all depends on Φ, also called *basis*, and on the inversion algorithm used to evaluate β.

In this project, 20 catheter points were used, equally spaced with steps of one voxel and pointing toward the tumor center (Figure 2.3). A custom Matlab function was employed to map their respective indices within the temperature vectors.

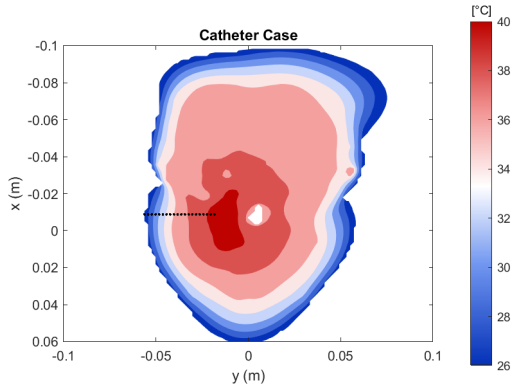

Figure 2.3: XY plane section of Yoon Sun neck, at Z = -0.005 m (tumor center). The color levels indicate the temperature of each pixel, while the catheter points are represented as black dots.

2.5.1 Inversion algorithms

The first step is to determine the solution β for Equation 2.6, which, for the sake of clarity, will be simplified here as $Ax = b$ (β is x). This can be achieved through various inversion algorithms; this section provides a description of the four that have been assessed.

The first is the Ordinary Least Squares (*LSQ*). This technique tries to find the set of values that minimizes the sum of squared errors, expressed as $||Ax - b||_2^2$ through the iterative algorithm called `lsqr`. It can be sensitive to noise, meaning that even small errors in the measurements can significantly affect the results.

The second method, Constrained Least Squares (*LSQLIN constraints*), adds additional conditions to the basic LSQ method. These constraints are enforced using the `lsqlin` Matlab function, which handles linear inequalities and equalities as follows:

$$\min_x \quad \|Ax - b\|_2^2 \quad \text{subject to} \quad \begin{cases} Cx \leq d, \\ C_{eq}x = d_{eq}, \\ l_b \leq x \leq u_b, \end{cases}$$

Where:

- A and b define the least squares objective $\|Ax - b\|_2^2$.
- C and d define the linear inequality constraints $Cx \leq d$, which were NOT imposed in our application.
- C_{eq} and d_{eq} define the linear equality constraints C_{eq} was set to a vector of ones and d_{eq} as the value 1. This ensures that the sum of all estimated contributions equals one, maintaining some kind of balance in the reconstruction.

- l_b and u_b are the lower and upper bounds on x, respectively. The lower bound was imposed as a vector of zeros, while the upper bound was not enforced; this ensures that the estimated temperatures cannot not be negative.

The third method, Tikhonov regularization (*Tikhonov*), addresses the instability of the LSQ solution by adding a "regularization" term to the equation. The modified equation becomes $||Ax - b||_2^2 + \mu||x||_2^2$, where μ is a parameter that controls the balance between the fitting of the data and the stability of the solution. This additional term, imposed equal to 13.35 in this thesis, penalizes large fluctuations in the estimated temperatures. This method is particularly useful when dealing with noisy data, as it reduces the risk of overfitting.

The fourth and most advanced method is L1-Regularization (*L1-Magic*), which focuses on promoting sparsity in the solution [31]. The idea is to find a β (x) with most of its values equal to zero or near zero, which translates to the possibility of having a patient temperature map very different from some temperature maps of the basis and very similar to some others. The optimization problem is formulated to find:

$$\min_x ||x||_1, \quad subject\ to\ ||Ax - b||_2 \leq \varepsilon, \tag{2.9}$$

where $||x||_1$ is the ℓ_1-norm of the solution and ε represents the allowable error in the reconstruction. In particular, the `l1qc_logbarrier`[2] function was used: it allows an initialization of the starting point and then iteratively updates the solution using Newton's method within the log-barrier framework. This barrier term becomes increasingly steep as the solution approaches the constraint boundaries, effectively guiding the solution towards the feasible region while minimizing the objective function. The barrier parameter τ is increased in each iteration to tighten the approximation of the ℓ_1- norm.

2.6 The parameters space

The space of the parameters is an N-dimensional space, with N being the number of tissues multiplied by the number of parameters considered. The selection of a set of dielectric (ε_r, σ) and thermal (k, w) parameters for all chosen tissues (*muscle, skin, fat and tumor*) translates to the definition of a point with a unique set of 16 coordinates (8 if considering only the thermal ones) inside a 16-D (8-D) hypercube whose boundaries are taken from the maximum and minimum values reported in the literature. This choice always leads to the generation of a specific temperature distribution. In this thesis, the ranges listed in Table 2.3 have been considered; to

[2]developed by Justin Romberg at Georgia Tech

highlight the discrepancy with the baseline values of the same tissues, Table 2.2 is also shown.

Table 2.2: Baseline parameter values for healthy tissues, from [19, 32, 33].

Tissue	ε_r [–]	σ [S m^{-1}]	k [W m^{-1}K^{-1}]	w [ml kg^{-1}K^{-1}]
Muscle	56.90	0.805	0.49	39.10
Fat	11.60	0.082	0.21	33.00
Skin	49.40	0.681	0.37	106.00
Tumor	59.00	0.890	0.51	72.30

Table 2.3: Min-Max parameter values for different tissues, from [19, 32, 33].

Tissue	ε_r [–]	σ [S m^{-1}]	k [W m^{-1}K^{-1}]	w [ml kg^{-1}K^{-1}]
Muscle	51.21-62.59	0.644-0.966	0.40-0.56	19.00-442.80
Fat	10.44-12.76	0.066-0.098	0.18-0.50	20.00-255.00
Skin	44.46-54.34	0.545-0.817	0.32-0.50	49.00-175.00
Tumor	53.10-64.90	0.712-1.070	0.41-1.50	36.15-848.00

Sobol distribution

Since the specific set of parameters belonging to the patient is unknown, every combination of parameters is equally likely, and therefore, the selection of a subset to build Φ should not be biased towards a specific region of the hyperspace. As a consequence, the Sobol distribution was used as the main sampling method (see Appendix A for details of the algorithm), varying the number of points as needed. The Sobol sequence is a low-discrepancy method designed to more uniformly cover high-dimensional spaces compared to purely random sampling. This ensures that sampling points are evenly distributed across all 16 (or 8) dimensions, minimizing gaps and clustering (e.g., Figure 2.4).

This thesis focuses on the two key pre-treatment elements of the reconstruction method: β and Φ. In fact, Chapter 3 explores the possibility of increasing the number of effective measurement points used to compute β. Since the number of catheter positions is inherently limited in a clinical setting, one way to improve reconstruction is to extract more information by integrating alternative sources of tissue-related data. In this part of the work the testing was carried out using the leave-one-out method: $B-1$ maps were used to reconstruct the left-out map, iteratively until all B basis maps were used as targets. Instead, Chapter 4 focuses on how the basis matrix Φ is built. Although the Sobol sequence is widely used for its ability to uniformly cover a parameter space, it does not necessarily guarantee the best outcome for all cases. The relationship between tissue properties and temperature distributions is complex, meaning that some regions of the parameter

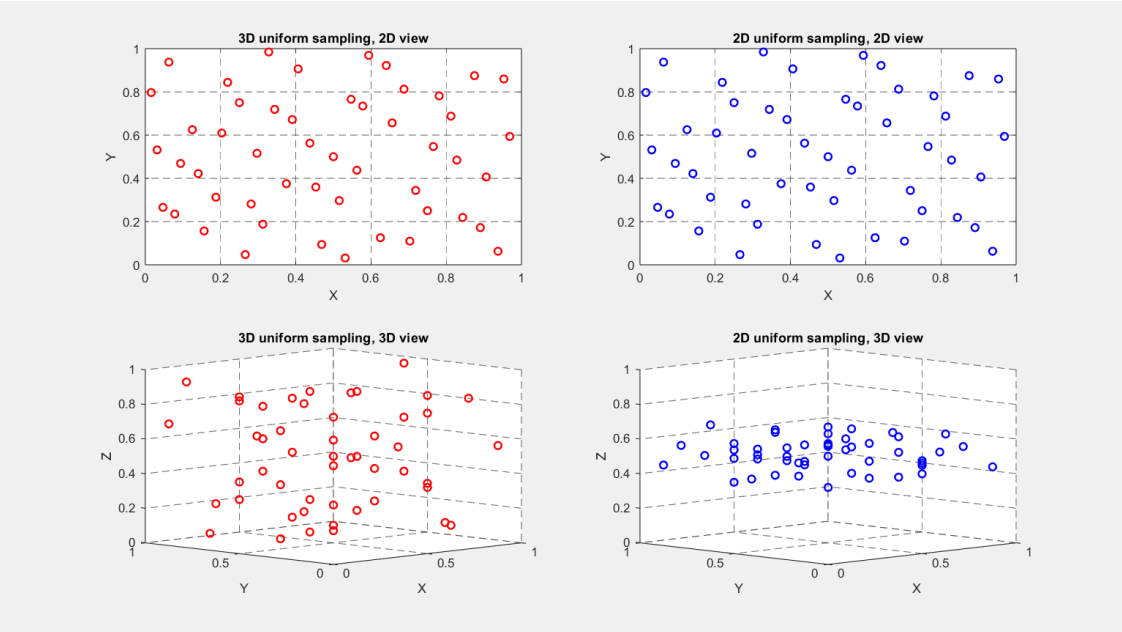

Figure 2.4: Example of sampling uniform in 2D, but not in 3D (bottom right). The same can happen by trying to sample uniformly tissue by tissue instead of all four tissue simultaneously

space may have a bigger impact on reconstruction accuracy than others. Instead of simply increasing the number of samples everywhere, targeted sampling strategies are explored such that coverage in those regions is improved and redundancy is avoided. These strategies focus on minimizing the Euclidean distance between the temperature maps or exploring areas that lead to a larger reconstruction error. Here, Φ_t was built using a Sobol distribution with $A = 500$. Ultimately, the goal is to build a more robust and reliable framework to estimate temperature distributions during hyperthermia treatments, minimizing the impact of uncertainties in tissue properties and measurement limitations.

Chapter 3

Active reflection coefficients implementation

The first goal simply consists in improving the inversion output β and thus the reconstruction, by adding measurement points from an alternative source. This source has to be non-invasive and assessable in a clinical setting, which is one of the reasons why the S parameters (or active reflection coefficients) were chosen.

3.1 Introduction

Before describing the implementation of the technique, it is important to explain why active reflection coefficients can be considered carriers of additional information; one must refer to the research field of microwave imaging [34] (MWI). MWI is a non-invasive modality for retrieving the geometrical and/or dielectric properties of objects (scatterers) embedded in an inaccessible domain through probing MW radiation; it has wide applications in non-destructive evaluation, medical imaging, remote sensing, seismic exploration, optics, atmospheric sciences, and other fields.

Consider an object occupying the volume V bounded by the surface S with a unit outer normal $\hat{n}$. This object of interest is embedded in a homogeneous background with dielectric constant ε_r^b. When an incident time-harmonic electromagnetic wave with electric field $\mathbf{E}^i(\mathbf{r})$ and angular frequency ω impinges on the object, one can measure the scattered field $\mathbf{E}^s(\mathbf{r})$ outside it. The purpose of MWI is to reconstruct the shape of the object (for a conductor) or the dielectric constant distribution $\varepsilon_r(\mathbf{r})$ of the object (for a dielectric) based on the measured scattered field. Starting with Maxwells equations as well as appropriate boundary conditions and using the Greens function technique, the following integral equations can be derived that link the scattered field to the property function of the object [35]:

For a Conductor:

$$\mathbf{E}^s(\mathbf{r}) = j\omega\mu \iint_S \overline{\overline{\mathbf{G}}}(\mathbf{r}, \mathbf{r}') \cdot \mathbf{J}^s(\mathbf{r}')\, dS', \quad \mathbf{r} \notin S \tag{3.1}$$

$$-\hat{n} \times \mathbf{E}^i(\mathbf{r_0}') = j\omega\mu\hat{n} \times \iint_S \overline{\overline{\mathbf{G}}}(\mathbf{r_0}, \mathbf{r}') \cdot \mathbf{J}^s(\mathbf{r}')\, dS', \quad \mathbf{r_0} \in S \tag{3.2}$$

For a dielectric:

$$\mathbf{E}^s(\mathbf{r}) = -k^2 \iiint_V \overline{\overline{\mathbf{G}}}(\mathbf{r}, \mathbf{r}') \cdot \left[\frac{\varepsilon_r(\mathbf{r})}{\varepsilon_r^b} - 1\right] \mathbf{E}(\mathbf{r}')\, dV', \quad \mathbf{r} \notin V \tag{3.3}$$

$$\mathbf{E}(\mathbf{r_0}) = \mathbf{E}^i(\mathbf{r_0}) - k^2 \iiint_V \overline{\overline{\mathbf{G}}}(\mathbf{r_0}, \mathbf{r}') \cdot \left[\frac{\varepsilon_r(\mathbf{r}')}{\varepsilon_r^b} - 1\right] \mathbf{E}(\mathbf{r}')\, dV', \quad \mathbf{r_0} \in V \tag{3.4}$$

Where:

- $\mathbf{J}^s$: Induced surface current density on the conductor.
- $\mathbf{G}$: Dyadic Greens function[1].
- $\mathbf{E}$: Total electric field in the dielectric object.
- μ: Magnetic permeability.
- k: Wave number of the background medium.

Equations 3.1 and 3.3 show the relationship between the incident fields, the scattered fields and the properties of the scatterer, which in the case of this thesis is the body model of Yoon-Sun. In both a real scenario and a simulated one, the overall change in the scattered field, linked to the change in the dielectric properties, can be measured. Therefore, the eight antennas are indirectly used as additional, non-invasive probes sensitive to the specific Sobol combination of parameters. This is where the active S-parameters or active reflection coefficients come into play. In general, the S-parameters of a scattering matrix S_{ij} provide a complete description of the network system as seen at its N ports, making it unnecessary to know what components comprise its interior [36]. S_{ij} is found by driving port j with an incident wave of voltage V_i^{inc} and measuring the scattered wave of amplitude V_i^{scat} coming out of port j:

$$S_{ij} = \frac{a_i^{scat}}{a_j^{inc}}, \quad fori, j = [1, N] \tag{3.5}$$

[1]Impulse response of an inhomogeneous linear differential operator defined in a domain with specified initial conditions or boundary conditions.

where:

$$a_i^{inc} = \frac{1}{2}\frac{V_i^{inc}}{\sqrt{Z_{0i}}} \tag{3.6}$$

$$a_i^{scat} = \frac{1}{2}\frac{V_i^{scat}}{\sqrt{Z_{0i}}} \tag{3.7}$$

with Z_{0i} = nominal matching impedance at port i, typically 50Ω.

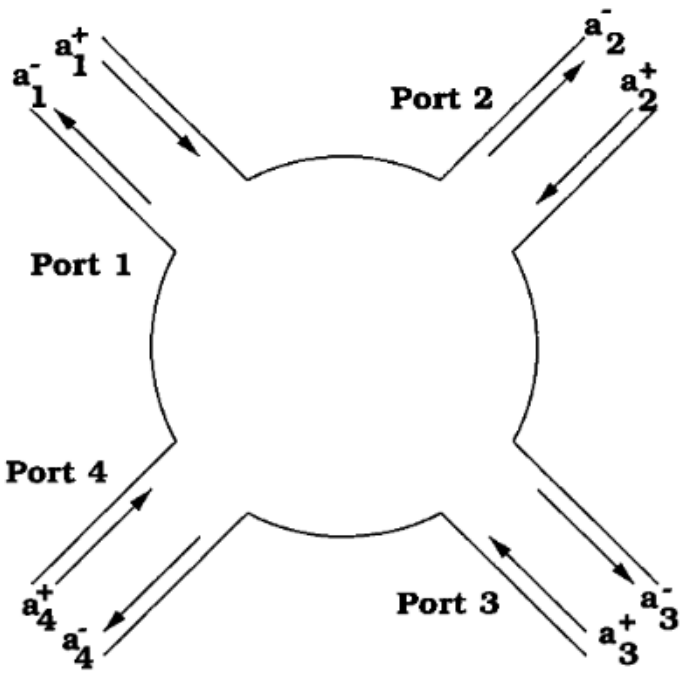

Figure 3.1: A general four-port microwave network, where forward (or incident) and backward (or scattered) waves are defined as a_{1-4}^{+} and a_{1-4}^{-}, respectively.

For example, consider the N-port network shown in 3.1; its associated scattering matrix is:

$$\begin{bmatrix} a_1^- \\ a_2^- \\ a_3^- \\ a_4^- \end{bmatrix} = \begin{bmatrix} S_{11} & S_{12} & S_{13} & S_{14} \\ S_{21} & S_{22} & S_{23} & S_{24} \\ S_{31} & S_{32} & S_{33} & S_{44} \\ S_{41} & S_{42} & S_{43} & S_{44} \end{bmatrix} \begin{bmatrix} a_1^+ \\ a_2^+ \\ a_3^+ \\ a_4^+ \end{bmatrix} \tag{3.8}$$

Notice that the self terms S_{ii} (diagonal elements of the scattering matrix) are the reflection coefficients associated with each port, and the off-diagonal terms $S_{ij|i\neq j}$ are the transmission coefficients [36]. The standard definition states that, to obtain such a matrix, a signal is injected into one port with all other inputs at all other ports set to zero. This implies that all the ports with no signals injected are match-terminated, so that no reflections occur. If this procedure is followed for all N ports, the standard scattering matrix is complete. However, when the circular array of

antennas must consider the "active" reflection coefficients, that are measured when all array elements are in place and excited [37]:

$$\Gamma_i^{active} = \frac{a_i^{scat}}{a_i^{inc}}, \quad when a_k = a_k^{exc} \forall k \tag{3.9}$$

$$\Rightarrow \Gamma_i^{active} = \sum_{k=1}^{N} S_{ik} \frac{a_k^{exc}}{a_i^{exc}} = S_{ii} + \sum_{k \neq i} S_{ik} \frac{a_k^{exc}}{a_i^{exc}} \tag{3.10}$$

It is to be noted that the active reflection coefficients are complex numbers and they depend on the frequency.

3.2 Extraction

A total of 75 unique parameter combinations were selected using the Sobol sequence in the 16-D parameter space. For each one of them, an EM simulation was performed in Sim4Life. A Python script (3.1) then automatically extracted the active reflection coefficients (RC) for each antenna.

Listing 3.1: Extraction of active reflection coefficients

```
# Reflection coefficients
for patch_num in range(1, 9):
        # Adding a new EmSensorExtractor
        em_sensor_extractor = simulation_extractor["Source␣
            {}␣␣(Patch␣{})".format(patch_num, patch_num)]
        document.AllAlgorithms.Add(em_sensor_extractor)

        # Adding a new ExcelExporter
        inputs = [em_sensor_extractor.Outputs["Reflection␣
            Coefficient(f)"]]
        excel_exporter= analysis.exporters.ExcelExporter(
            inputs=inputs)
        excel_exporter.FileName = (dir_RC + "RC{}_Patch{}.
            xlsx".format(i, patch_num))
        excel_exporter.UpdateAttributes()
        document.AllAlgorithms.Add(excel_exporter)
        excel_exporter.Update(overwrite=True)
        excel_exporter.Update(overwrite=True)
```

Following this, thermal simulations were conducted and the corresponding temperature maps used to construct the Φ matrix were extracted. The extracted RC data for each antenna was stored in a 5002×3 Excel table. The first column

listed frequencies ranging from 384 MHz to 484 MHz in 0.02 MHz increments. The second and third columns contain the real and imaginary parts of the RC, respectively. To isolate the relevant values, the row corresponding to the working frequency (434 MHz) was extracted with a custom code (3.2).

Listing 3.2: Extraction of real and imaginary parts of the RC at 434 MHz

```
function FromExcelToMat(B)
% Function to extract the S - active parameter at 434 MHz
    for each
% antenna and each Sobol set of parameters

% inputs:
% - B = total number of Sobol sets considered
% Outputs:
% - S_active.mat = 16 x B matrix contaning the active
    reflection
%                  coefficients at the working frequency

filepath = cd + "\Refl_coeff";
S = zeros(16, B);

tic
for i = 1 : B
    for j = 1 : 8
        if isfile(strcat(filepath, '\RC',num2str(i),'_Patch
            ', num2str(j), '.xlsx'))
            RCtable = readtable(strcat(filepath, '\RC',
                num2str(i),'_Patch', ...
                 num2str(j), '.xlsx'), VariableNamingRule="
                    preserve");
            RC = table2array(RCtable);
        else
            disp("Error: there aren't as many combinations
                of parameters " + ...
                 "as you think")
        end
        %select only the values at 434 MHz (index 2501)
        S(j, i) = RC(2501, 2);
        S(j+8, i) = RC(2501, 3);
    end
end
toc
```

```
save("S_active.mat", "S");

end
```

These values are then concatenated to form a 16-element feature vector for each iteration:

$$S(:,j) = \begin{bmatrix} \Re\{RC_1\} \\ \Re\{RC_2\} \\ \vdots \\ \Re\{RC_8\} \\ \Im\{RC_1\} \\ \Im\{RC_2\} \\ \vdots \\ \Im\{RC_8\} \end{bmatrix}_j \quad , \quad example: S(:,1) = \begin{bmatrix} -0.1945 \\ -0.2416 \\ 0.0098 \\ -1.1384 \\ 0.1464 \\ -0.0313 \\ 0.1666 \\ -0.1821 \\ 0.1535 \\ -0.1455 \\ -0.3213 \\ -3.6487 \\ -0.1888 \\ -0.4107 \\ -0.0858 \\ -0.2031 \end{bmatrix} \tag{3.11}$$

where $S(:,j)$ represents the feature vector corresponding to the j-th iteration, with the first eight elements containing the real parts of the reflection coefficients and the last eight containing the imaginary parts. An example of the first column of the S-matrix is given. The S matrix is concatenated to the matrix Φ evaluated in the catheter indexes, creating a matrix with dimensions $[36 \times 75]$:

$$\begin{bmatrix} \Phi|_{catheter\ points} \\ S \end{bmatrix} \times \beta = \begin{bmatrix} f|_{catheter\ points} \\ S^f \end{bmatrix} \tag{3.12}$$

Where S^f stands for the S-active parameters related to the target map's set of parameters (only one column).

3.3 Accuracy analysis

This study evaluated the accuracy of the reconstruction with and without the inclusion of the S matrix in a combination of different scenarios, resulting in a total of 64 cases. The scenarios are structured as follows:

- Four inversion methods (described in 2.5.1).
- Two catheter directions of insertion (x and y directions along the transversal plane).
- Two sets of measurement points (the limited subset of 20 catheter points vs. the entire ROI [2]).
- Noise-free measurements vs. addition of Gaussian noise (standard deviation $\sigma = 0.2°C$ and mean $\mu = \pm\ 0.1°C$), with 100 positive realizations and 100 negative realizations for each target map.

In order to have a comprehensive view of performance and compare all different cases, some custom metrics were created and used along with the T_{50}, which is a clinically relevant parameter to determine the quality of hyperthermia [38].

3.3.1 Goodness, likelihood and error thresholds

The goodness function is defined as the percentage of voxels whose reconstructed temperature has an error lower than a certain threshold:

$$g(\psi, \chi) = \frac{Vol(\mathbf{r} \in A : |\hat{f}(\mathbf{r}; \psi) - f(\mathbf{r}; \psi)| \leq \chi)}{Vol(A)} \cdot 100 \tag{3.13}$$

where χ °C is the error threshold and $A = ROI \subset \mathbb{R}^3$ represents the set of mesh points where the temperature map is evaluated. $\hat{f}(\mathbf{r})$ is the reconstructed temperature map, while $f(\mathbf{r}; \psi)$ is the target map corresponding to a given set of pseudo-random parameters ψ. According to its definition, $g = 100$ denotes a perfect (ideal) reconstruction. Repetition of the reconstruction for a large number of target maps yields a matrix of goodness values, where each row represents a different target temperature map, and each column corresponds to a specific error threshold.

Among all the considered cases, the likelihood function quantifies the probability that at least a percentage ζ of the ROI exhibits an error lower than a specified

[2] Ideal case which sets the upper limit in the accuracy of the reconstruction under the same combination of experimental conditions

threshold χ:

$$e(\zeta, \chi) = \frac{\sum\{g(\psi, \chi) : g(\psi, \chi) \geq \zeta\}}{m_t} \tag{3.14}$$

In other words, the fraction of target maps whose reconstruction meets a certain goodness is computed for each threshold. In those trials were noise was added, m_t in Equation 3.14 has to be multiplied by the number of noise realizations, for a total of 15000 reconstructions.

The key estimator in this study is χ_{95}, defined as the minimum error threshold achieved by at least 95% of the ROI with a 95% probability:

$$\chi_{95} = \min_{\chi} \quad e(95, \chi) > 0.95 \tag{3.15}$$

The error thresholds ranged from 0 °C to 1.5 °C with a spacing of 0.02 °C. It should be noted that this metric is particularly stringent as it focuses not only on a broad spatial accuracy but also on a high level of certainty.

As shown in Table 3.1 and Table 3.2, χ_{95} exhibits minimal sensitivity to the inclusion of S-parameters. In the noise-free case, LSQR achieves the lowest χ_{95} (0.3 °C in the x direction), followed by *Tikhonov* and *LSQR* (0.9 °C), while *LSQLIN constraints* yields the highest values (1.2 °C in the y direction, 0.9 °C in the x direction). In noisy conditions, *LSQR* and *L1 magic* χ_{95} exceeded the maximum error threshold. *Tikhonov* remains the best choice, achieving 0.9 °C in the x direction and 1.10 °C in the y direction. *LSQLIN constraints* follows with slightly higher values (0.96 °C in the x direction, 1.18 °C in the y direction).

Table 3.1: $\mathcal{X}_{95}$ $[°C]$ using 20 catheter measurements without noise. The reconstruction using the whole ROI yielded a $\mathcal{X}_{95}$ of 0.06, 0.4, 0.08 °C for the *LSQR*, *LSQLIN constraints* and *Tikhonov* methods[a], respectively, regardless of S and direction.

Method	**DIR. Y**		**DIR. X**	
	Without S	With S	Without S	With S
LSQR	0.98	0.98	0.3	0.36
LSQLIN constraints	1.20	1.22	0.9	0.96
Tikhonov	1.08	1.08	0.9	0.9
L1 magic	1.02	1.0	0.9	0.92

[a] *L1 magic* results in the whole ROI couldn't be estimated due to the algorithm need to generate matrices exceeding storage capacity.

Table 3.2: $\mathcal{X}_{95}$ [°C] with Gaussian noise added to the 20 catheter measurements. The reconstruction using the whole ROI yielded a $\mathcal{X}_{95}$ of 0.14, 0.44, 0.16 °C for the *LSQR*, *LSQLIN constraints* and *Tikhonov* methods[a], respectively, regardless of S and direction.

Method	**DIR. Y**		**DIR. X**	
	Without S	With S	Without S	With S
LSQR	> 1.5	> 1.5	> 1.5	> 1.5
LSQLIN constraints	1.18	1.18	0.96	0.94
Tikhonov	1.10	1.10	0.9	0.9
L1 magic	> 1.5	> 1.5	> 1.5	> 1.5

3.3.2 Temperature in the tumor and healthy tissues

The T_{50} is defined as the median temperature in the tumor volume and it was used in this differential formulation:

$$\Delta T_{50} = |T_{50} - \hat{T}_{50}| \tag{3.16}$$

where T_{50} is the median temperature of the tumor in the target map and $\hat{T}_{50}$ is the median temperature of the tumor in the reconstructed target map. The ΔT was also evaluated, defined as the median of the absolute difference between the target map and the reconstructed map on the entire ROI.

$$\Delta T = median(|f_{|whole\ ROI} - \hat{f}_{|whole\ ROI}|) \tag{3.17}$$

These metrics too were evaluated for each target map and then their median was computed across the entire test set (75 reconstructions in the noiseless scenarios and on 15000 reconstructions in the noisy scenarios), in order to have a unique representative value for each scenario.

The effect on ΔT is more pronounced than on χ_{95} (Table 3.3 and Table 3.4). Without noise, *LSQR* in the x direction achieves the lowest ΔT (0.0318 °C), followed closely by *LSQLIN constraints* (0.0470 °C). In noisy conditions, the performance of *LSQR* deteriorates drastically, reaching 4.7878 °C in the x direction, although the S parameters help mitigate this, reducing it to 1.7162 °C. *LSQLIN constraints* in the x direction emerges as the best choice (0.0877 °C without S, 0.0729 °C with S), maintaining a low error even in noisy conditions. *Tikhonov* and *L1 magic* perform worse, with values exceeding 0.13 °C and 4.40 °C, respectively.

For ΔT_{50} the differences in noise-free conditions are minor, with *LSQLIN constraints* in the x direction (0.2953 °C) yielding the best performance, followed by *Tikhonov* (0.3390 °C) and *LSQR* (0.3432 °C). However, under noise, *LSQR* in

Table 3.3: ΔT [$^{\circ}C$] using 20 catheter measurements without noise. The reconstruction using the whole ROI yielded a ΔT of 0.0053, 0.0251, 0.0085 °C for the *LSQR*, LSQLIN constraints and *Tikhonov* methods[a], respectively, regardless of S and direction.

Method	**DIR. Y**		**DIR. X**	
	Without S	With S	Without S	With S
LSQR	0.0802	0.0712	0.0318	0.0285
LSQLIN constraints	0.0885	0.0826	0.0470	0.0435
Tikhonov	0.1315	0.1327	0.0917	0.0911
L1 magic	0.2270	0.2094	0.1719	0.1670

Table 3.4: ΔT [$^{\circ}C$] with Gaussian noise added to the 20 catheter measurements. The reconstruction using the whole ROI yielded a ΔT of 0.1000, 0.0549, 0.1001 °C for the *LSQR*, LSQLIN constraints and *Tikhonov* methods[a], respectively, without S, regardless of the direction. With S, the whole ROI results were 0.0999, 0.0475, 0.1001 °C respectively

Method	**DIR. Y**		**DIR. X**	
	Without S	With S	Without S	With S
LSQR	2.679	1.0144	4.7878	1.7162
LSQLIN constraints	0.0983	0.0944	0.0877	0.0729
Tikhonov	0.1606	0.1704	0.1355	0.1314
L1 magic	4.4446	3.6903	5.9377	4.4036

the x direction completely breaks down, producing extreme errors of 15.3122 °C, even though S-parameters improve it to 6.9412 °C. *LSQLIN constraints* in the x direction, on the other hand, remains highly stable (0.3279 °C without S, 0.3053 °C with S), making it the best choice for the estimation of tumor temperature. *Tikhonov* follows closely behind (0.3402 °C), but *LSQR* remains too unreliable for clinical use.

Table 3.5: ΔT_{50} [$^{\circ}C$] using 20 catheter measurements without noise. The reconstruction using the whole ROI yelded a ΔT_{50} of 0.0163, 0.02544, 0.0582 °C for the *LSQR*, LSQLIN constraints and *Tikhonov* methods[a], respectively, regardless of S and direction

Method	**DIR. Y**		**DIR. X**	
	Without S	With S	Without S	With S
LSQR	0.0187	0.0192	0.3432	0.3121
LSQLIN constraints	0.031	0.0299	0.2953	0.2834
Tikhonov	0.0578	0.0575	0.339	0.3369
L1 magic	0.0762	0.0783	0.2694	0.2789

Table 3.6: ΔT_{50} with Gaussian noise added to the 20 catheter measurements. The reconstruction using the whole ROI yielded a ΔT_{50} of 0.1002, 0.2603, 0.1010 °C for the *LSQR*, LSQLIN constraints and *Tikhonov* methods[a], respectively, without S, regardless of the direction. With S, the whole ROI results were 0.1000, 0.2602, 0.1010 °C respectively

Method	**DIR. Y**		**DIR. X**	
	Without S	With S	Without S	With S
LSQR	0.9759	0.4007	15.3122	6.9412
LSQLIN constraints	0.1195	0.1195	0.3279	0.3053
Tikhonov	0.1128	0.1125	0.3427	0.3402
L1 magic	0.9276	1.3419	33.5112	53.5681

Chapter 4

Optimized sampling in the parameters space

4.1 Introduction

The Sobol distribution offers an excellent foundation for exploring various combinations of tissue parameters due to its uniform coverage of high-dimensional spaces. However, that same uniformity can also become a limitation. Despite simplifying assumptions, the relationship between the temperature distribution and the properties of the tissue in a heterogeneous region such as the head and neck (H&N) remains very complex. As a result, two parameter sets very close in a particular region of the parameter space may yield markedly different temperature maps and vice versa. This was already evident in the first part of this work, where a single EM simulation was performed with the baseline values of the dielectric parameters and an initial Sobol distribution of 30 unique combinations (ξ_{30}) of thermal parameters for the four mentioned tissues (8-D parameter space) used to create just as many temperature maps. The function `pdist` in Matlab was used to calculate the distance between each pair of combinations and maps, respectively; in particular, the standardized Euclidean distance was chosen for ξ_{30} and the Euclidean distance for Φ. The Euclidean distance between the i-th temperature map and the j-th one, with $i, j = [1 : 30]$, is defined as the norm of the euclidean vector difference:

$$d(\Phi(\mathbf{r};\xi_i), \Phi(\mathbf{r};\xi_j)) = ||\Phi(\mathbf{r};\xi_i) - \Phi(\mathbf{r};\xi_j)|| \tag{4.1}$$

The standardized euclidean distance follows the same definition, but each coordinate difference between observations is scaled by dividing by the corresponding element of the standard deviation. Standardization is needed because in the parameter space the two coordinates have very different magnitudes, with w ranging

from 19 to 848 [ml $kg^{-1}K^{-1}$] and k ranging from 0.18 to 1.5 [W $m^{-1}K^{-1}$]. The distances can be visualized as the following matrix:

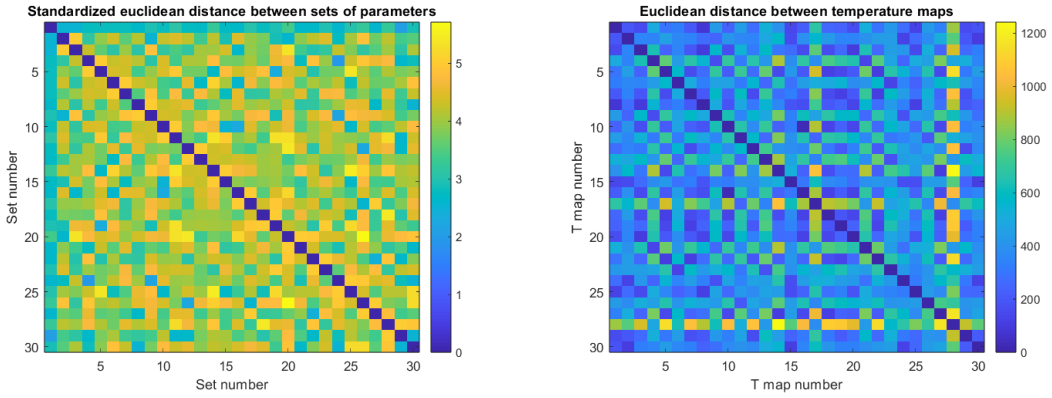

(a) (b)

Figure 4.1: Standardized euclidean distance [−] between initial batch of 30 Sobol sets of parameters (a) and euclidean distance [°C] between their respective temperature maps (b). The diagonal is nil as the distance between one map and itself is, by definition, equal to zero.

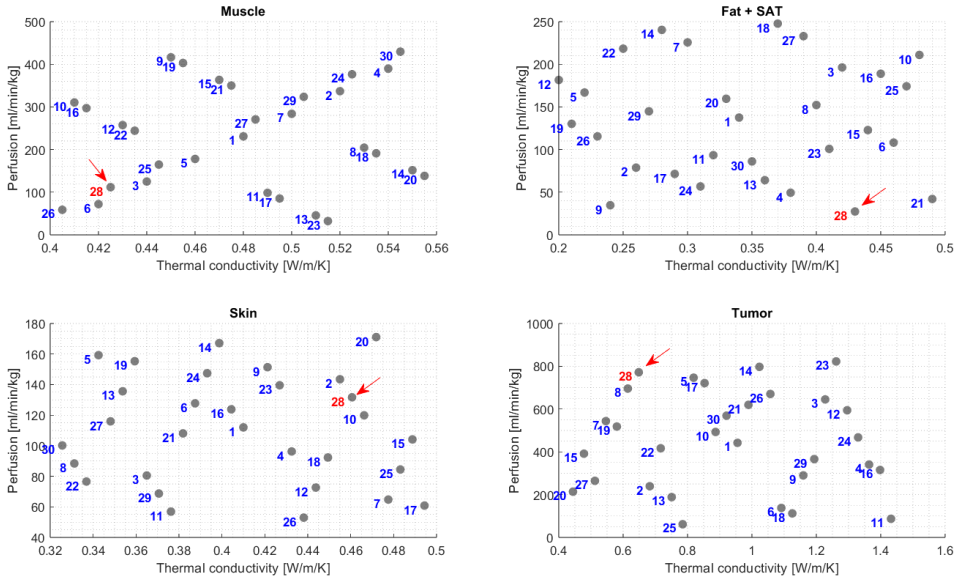

Figure 4.2: Distribution of the thermal parameters in each tissue

It was observed that the temperature map n.28 (and n.17) had a large distance from many of the other maps, although the corresponding set of parameters is not

"far" from the others. Figure 4.2 may provide a clearer visualization.

The reconstruction of a map generated by parameters located in these high-gradient regions (in the example, near distribution n.28) is likely to be inaccurate due to the insufficient representation of that region within the basis matrix Φ built using Sobol sequences. A straightforward approach might be to increase the number of sampling points throughout the parameter space, but this would not produce better results, as the basis matrix would be cluttered with "useless" information; this was demonstrated by a previous research [39], where an SVD analysis of Φ revealed a plateau in the magnitude of its eigenvalues, indicating diminishing returns in information gain when using more than 50 to 70 Sobol points. This redundancy is also evident in Figure 4.1 where the sets generally have the same distance between them, but the temperature maps do not, with many "close" to each other in the temperature space.

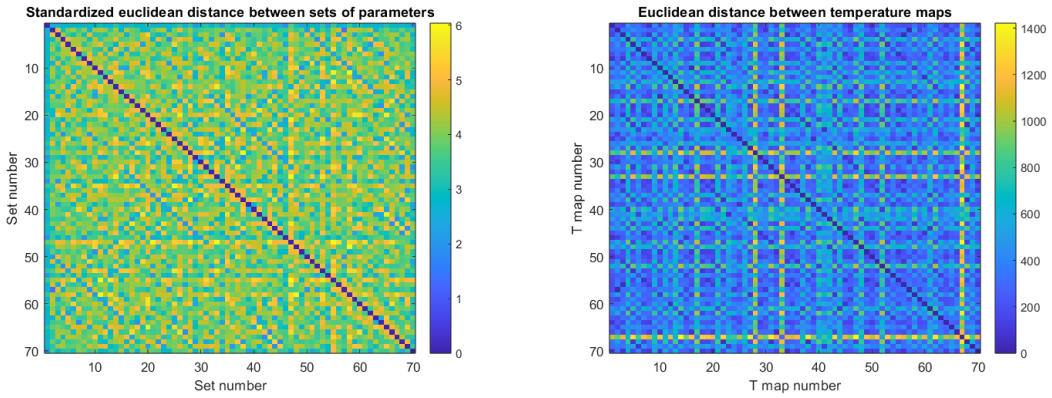

(a) (b)

Figure 4.3: Standardized euclidean distance [−] between 70 Sobol sets of parameters (a) and euclidean distance [$°C$] between their respective temperature maps (b).

This behavior led us to choose new sets in a targeted way, allowing them to cluster or disperse in some regions rather than always imposing uniformity. It must be specified that the Sobol sequence was still used, but after iteratively questioning the temperature space and subsequently restricting the algorithm's area of effect. As a reference to compare the efficacy of this optimization, 40 sets and maps were chosen with Sobol and used together with the 30 mentioned sets and maps to build a 'standard' Φ, the distance matrix of which is shown in Figure 4.1.

4.2 Target refinement strategies

The basis construction process was implemented in MATLAB, where the following sequence of steps was executed in each iteration:

1. Check if, in the folder where the temperature maps are stored, there were more than 70 maps. If there were, it maintained the first 30 (initial Sobol ones) and randomly selected 40 from the remaining, then saved that specific basis Φ. If there were not, select n temperature maps with either method, stored their indexes and selected the respective sets of thermal parameters.

2. Create n "bounding boxes" (8D hypercubes) surrounding each couple of selected points in the parameter space, leaving a margin d (fraction of a range which depends on the method), for each tissue and always within some boundaries defined by the min-max values found in literature (4.1).

Listing 4.1: bounding box creation

```
    % Read boundaries from Excel file -> otherwise the
       new ranges may not respect the literature values
    boundary_file = ''Parameters.xlsx'';
␣␣␣␣x_boundaries␣=␣readmatrix(boundary_file,␣...
␣␣␣␣␣␣␣␣...'Sheet', 3, 'Range', 'C2:D5'); % k boundaries
    y_boundaries = readmatrix(boundary_file, ...
        ...'Sheet', 4, 'Range', 'C2:D5'); % w boundaries

    for j=1:n
        for i = 1:size(column_pairs, 1)
            col_x = column_pairs(i, 1); % k column
               indexes
            col_y = column_pairs(i, 2); % w column
               indexes

            X_data = therm_par(:, col_x); % k values
            Y_data = therm_par(:, col_y); % w values

            % Extract boundaries for the current tissue
            x_min_boundary = x_boundaries(i, 1);
            x_max_boundary = x_boundaries(i, 2);
            y_min_boundary = y_boundaries(i, 1);
            y_max_boundary = y_boundaries(i, 2);

            x_min = min(X_data(i0(j)), X_data(i1(j)));
            x_max = max(X_data(i0(j)), X_data(i1(j)));
```

```
            y_min = min(Y_data(i0(j)), Y_data(i1(j)));
            y_max = max(Y_data(i0(j)), Y_data(i1(j)));

            % Add a margin, respecting the boundaries
            margin_x = d * (x_max - x_min);
            margin_y = d * (y_max - y_min);

            bounding_boxes{j}(i, :) = ...
                ...[max(x_min - margin_x, x_min_boundary
                    ), ...
                    min(x_max + margin_x, x_max_boundary)];
            bounding_boxes{j}(i+4, :) = ...
                ...[max(y_min - margin_y, y_min_boundary
                    ), ...
                    min(y_max + margin_y, y_max_boundary)];
        end
    end
```

3. Generate k additional Sobol values within each bounding box (4.2).

Listing 4.2: New batch creation

```
    % Quasi random Sobol sequence %
    q = qrandstream('sobol',numel(param)*numel(tissues)
        ,...
            ...'Skip',1);

    for j = 1:n
    % generates k numbers from the flux of semi-random
    %numbers q. Then use them as coefficients for the
    %ranges and them to the minimum values
    X = rand(q,k,numel(param)*numel(tissues));

    for i = 1:length(bounding_boxes{j})
        NewBatch(k*(j-1)+1:k*j,i) = bounding_boxes{j}(i
            ,1)...
             ...+range(bounding_boxes{j}(i,:)).*X(:,i);
    end

    end
```

4. Perform the thermal simulation in Sim4Life imposing the newly found thermal conductivity and perfusion values for each tissue. As source for the stationary

thermal simulation, the power density obtained with the baseline dielectric parameters for all the tissue was used.

5. Save the temperature maps in a specific folder.

The three optimized bases, Maximum Sum of Distances (MSD), Largest Minimum Distances (LMD) and Maximum Error Leave-One-Out (MELOO), share this building process, only differing in how they select the regions to refine in the first step.

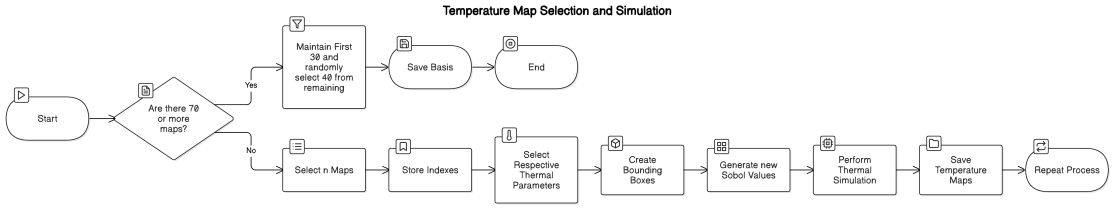

Figure 4.4: Optimization flowchart with key steps

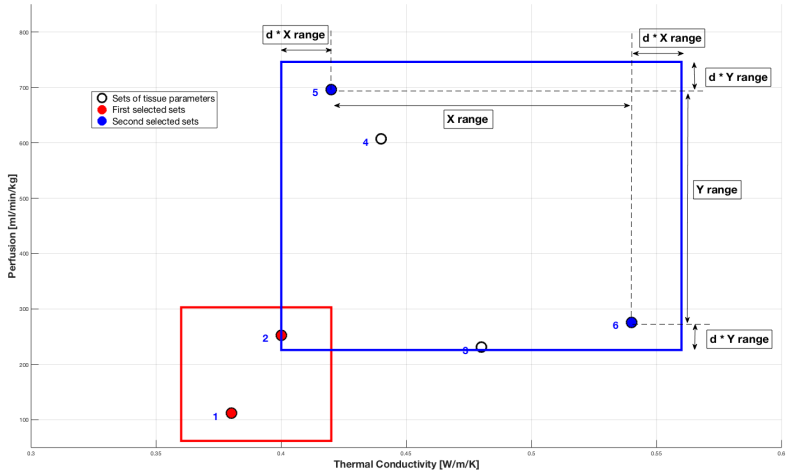

Figure 4.5: Example: bounding boxes creation in the parameter space, for a single tissue. Visualization of the margins using d.

To explore the influence of the optimization variables n, d and k, two values were used for each variable, resulting in eight different bases for each method and a total of 24 bases, plus the Sobol one for comparison. In particular:

- n was either 1 or 5
- d was either 10% or 50% of the range of the selected pair of sets for the LMD and MSD methods (Figure 4.5), 10% or 50% of the range of properties for that tissue for the MELOO method.
- k was either 5 or 8.

For each method, two examples of how the points were added during the iterations of the algorithm are shown, as well as two examples of the final distance matrices.

4.2.1 Maximum Sum of Distances method

The Maximum Sum of Distances is the most intuitive method, prioritizing maps that have the highest overall distance from the rest. This prevents parameters from being added in regions where the temperature space already has sufficient coverage, preferring the ones where the outcome of the thermal simulations appears to be very sensitive to the parameters variation.

Listing 4.3: MSD initial selection of maps

```
% Compute pairwise Euclidean distances
D = pdist(Phi', 'euclidean');

% Convert distances to a squareform matrix
squareD = squareform(D);

% copy squareD
temp=squareD;
% change diagonal made of zeros
temp(1:size(squareD, 1)+1:end) = Inf;

% sum on the rows
sum_distances = sum(squareD, 2);

% select max sum of distances
[~, ind_sum] = sort(sum_distances, 'descend');
i0(1,:) = ind_sum(1:n);

% select neighbors
for j = 1:n
    [~, i1(j)] = min(temp(i0(j), :), [], 2);
end
```

The selection in the first step of the algorithm is carried out as shown in 4.3, explained as follows:

a) evaluate the sum of the distances between each map and the others

b) find the indices of the n largest sums of distances

c) find the indices of their closest temperature maps, respectively.

As already described, those indexes will then be used to pinpoint the related sets of parameters and generate new ones. If the new parameters produce temperature maps near the previously selected ones, then those maps will not be selected anymore. If there are still maps with the maximum sum of distances in that same region, it means that increasing the points in the related parameter space still has not provided enough coverage of that particular temperature space. Thus, another iteration will be performed there.

Example: MSD n=1, d = 0.1, k = 8

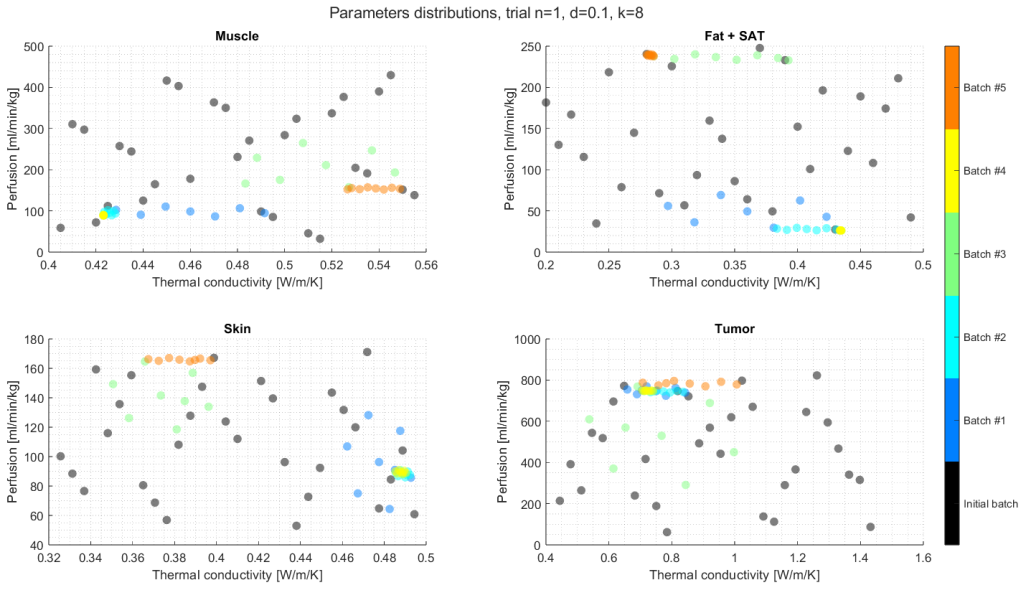

Figure 4.6: Final parameter distribution, for each tissue, for the MSD basis created with n=1, d = 0.1, k = 8. Each color represents a different batch.

Figure 4.6 shows a color-coded scatter plot of how the parameters were added in each iteration (batch), while Figure 4.7 shows an example of bounding box created during one of the iterations.

Figure 4.2.1 shows a distance matrix that is very different from the one obtained with plain Sobol. Both the parameters distances and the temperature ones exhibit a larger number of yellow cells and a brighter shade of yellow, indicating a higher number of maps found with a higher distance (more isolated). Blue areas are also more present, but it is not surprising: it indicates that the maps and parameters that are within the same bounding box have a small distance. This characteristic is particularly noticeable in the MSD method and, in general, when the margin d is on the lower range and k is on the higher range, since it leads to more crowded bounding boxes.

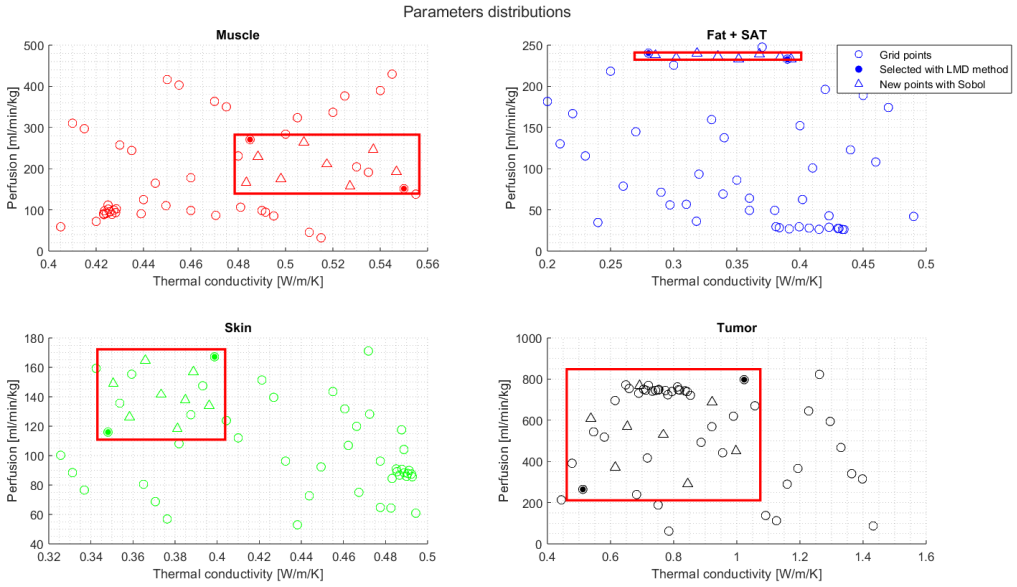

Figure 4.7: Bounding boxes created during the third iteration with n=1, d = 0.1, k = 8

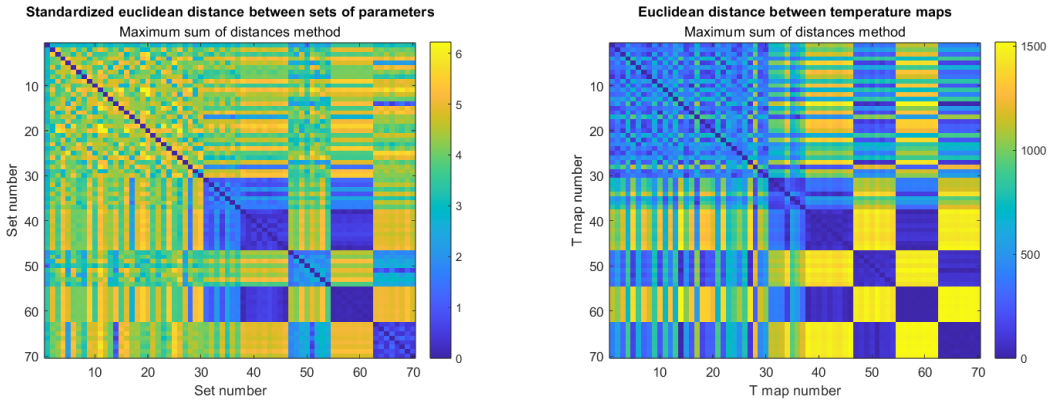

(a) (b)

Figure 4.8: Standardized euclidean distance [−] between sets of parameters (a) obtained with MSD, n=1, d=0.1, k = 8 and euclidean distance [°C] between their respective temperature maps (b).

Example: MSD n=5, d = 0.1, k = 5

For this second example with a higher initial number of selected maps, the final color-coded distribution is shown in Figure 4.9.

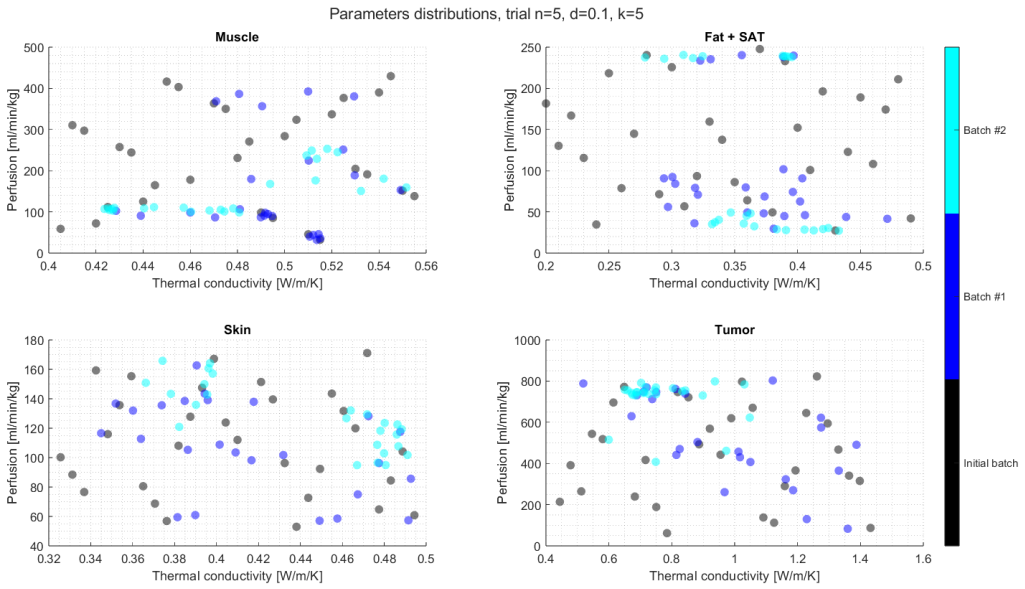

Figure 4.9: Final parameter distribution for the MSD basis created with n = 5, d = 0.1 and k = 5. Each color represents a different batch.

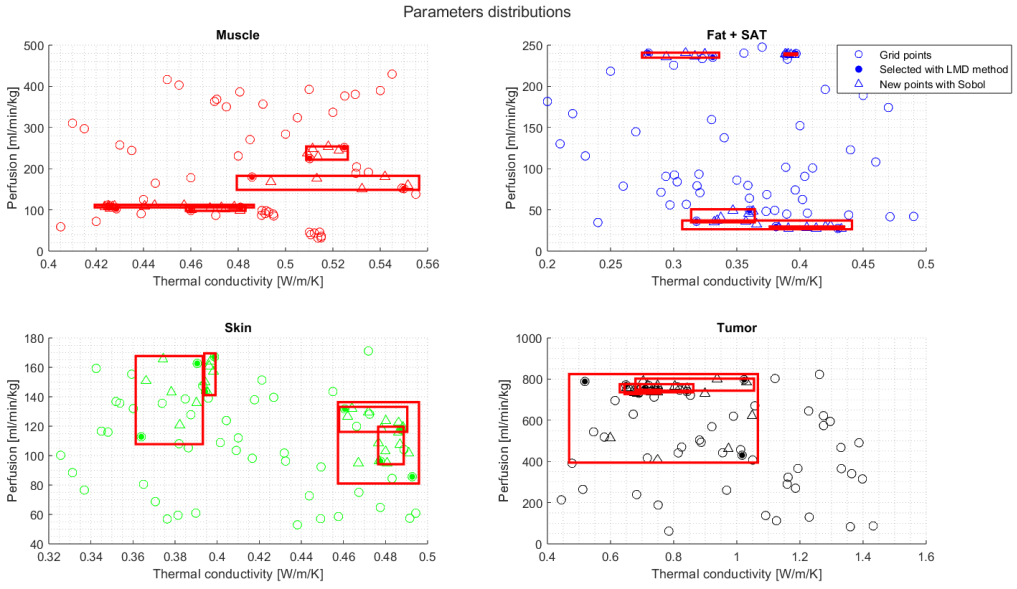

Figure 4.10: Bounding boxes created during the second iteration with MSD, n=5, d=0.1, k=5

In this example (Figure 4.2.1, the crowding is less present; however, the magnitude of the distances is lower with respect to MSD with n = 1, d = 0.1 and k =

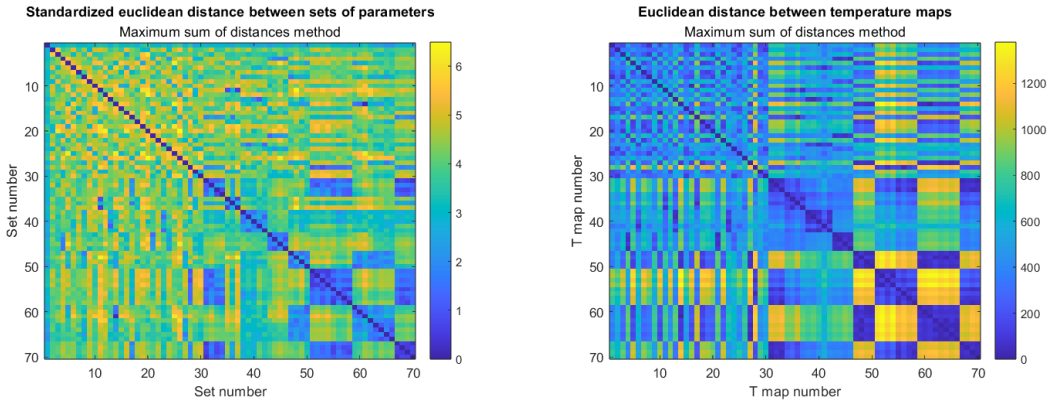

(a) (b)

Figure 4.11: Standardized euclidean distance [−] between sets of parameters (a) obtained with MSD, n = 5, d = 0.1, k = 5 and euclidean distance [°C] between their respective temperature maps (b).

8 (approximately 1350 °C vs. 1500 °C). This suggests that the method identified parameter sets with closer temperature maps.

4.2.2 Largest Minimum Distances method

The LMD method is similar to the MSD one, but is more strict, focusing on those maps that are the most different from their closest neighbor; this translates to maps that are the most isolated in absolute terms. For example, in the simplification

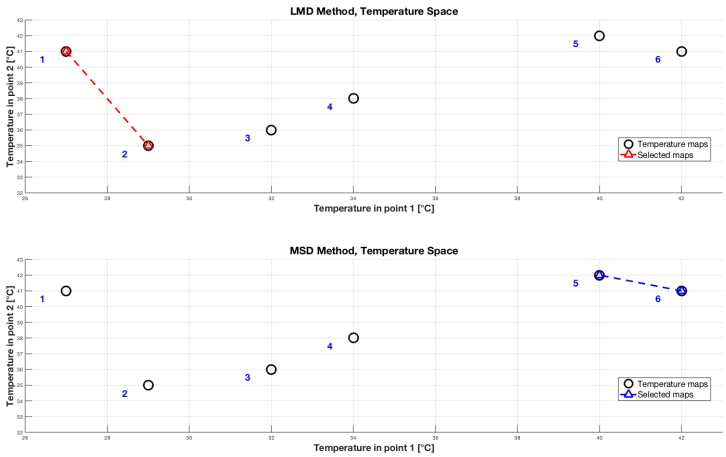

Figure 4.12: Example of MSD and LMD different selection criteria in a 2D simplification of the temperature space. Maps 1 and 2 selected by the LMD method (upper plot), maps 5 and 6 selected by the MSD method (lower plot)

shown in Figure 4.12, maps 5 and 6 are selected by the MSD method because they are the most distant overall, although they are close to each other. In contrast, by the LMD interpretation, the exploration of that region is not a priority because it is already represented by two points. Instead, point 1 is pinpointed as the only representative of its region and thus worth of additional neighbors.

Listing 4.4: LMD initial selection of maps

```
% Compute pairwise Euclidean distances
D = pdist(Phi', 'euclidean');
% Convert distances to a squareform matrix
squareD = squareform(D);

% copy squareD
temp=squareD;
% change diagonal made of zeros
temp(1:size(squareD, 1)+1:end) = Inf;

% evaluate minimum distances for each tmap (excluding
%themselves)
```

```
min_distances = min(temp, [], 2);

% find the index of the tmaps with the
% largest minimum distance
[~, ind_min] = sort(min_distances, 'descend');
i0(1,:) = ind_min(1:n);

% find their respective nearest neighbour
for j = 1:n
[~, i1(j)] = min(temp(i0(j), :), [], 2);
end
```

The selection is carried out as shown in 4.4, detailed as follows:

1. evaluate the minimum distances in the temperature space, excluding the diagonal.
2. Find the indices of the n largest minimum distances.
3. find the indexes of their closest temperature maps, respectively.

Example: LMD n=1, d = 0.1, k = 5

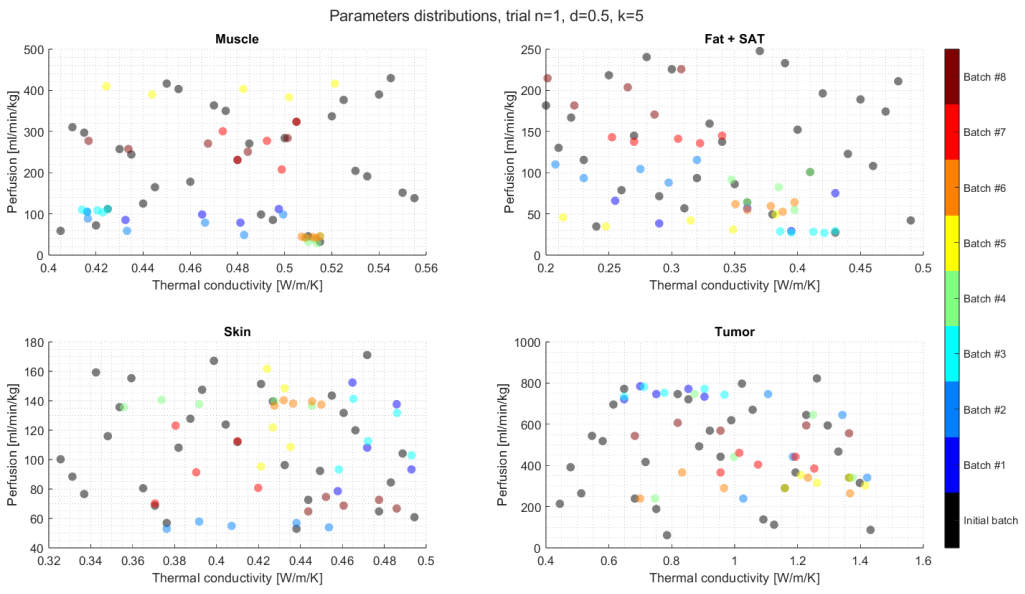

Figure 4.13: Final parameter distribution for the LMD basis created with n = 1, d = 0.1 and k = 5. Each color represents a different batch.

With a number of new points for each bounding box equal to 5, and a number

of initial selected maps equal to 1, the number of batches increases to 8, as shown in figure 4.13.

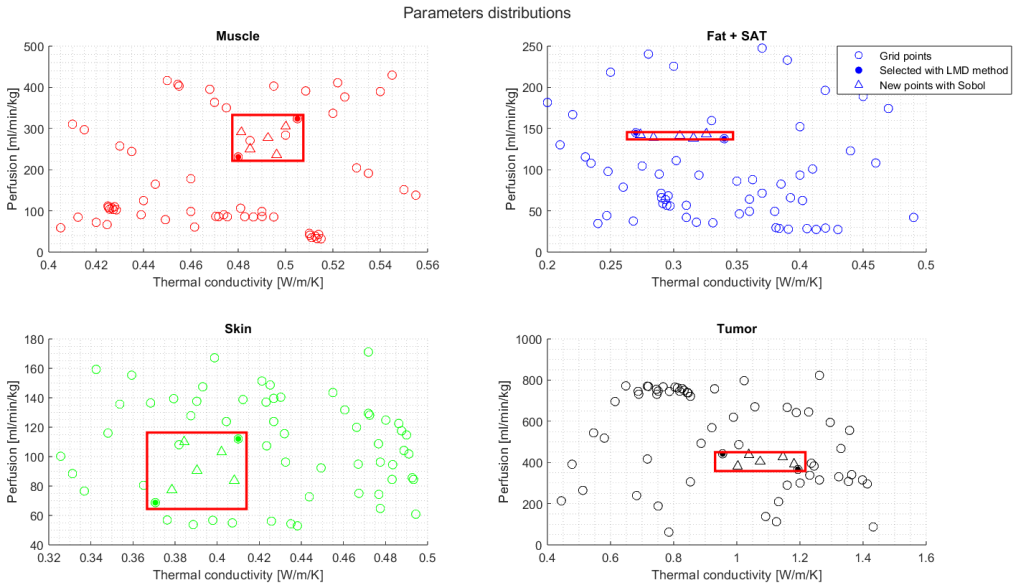

Figure 4.14: Bounding boxes created during the seventh iteration with LMD, n=1, d=0.1, k=5

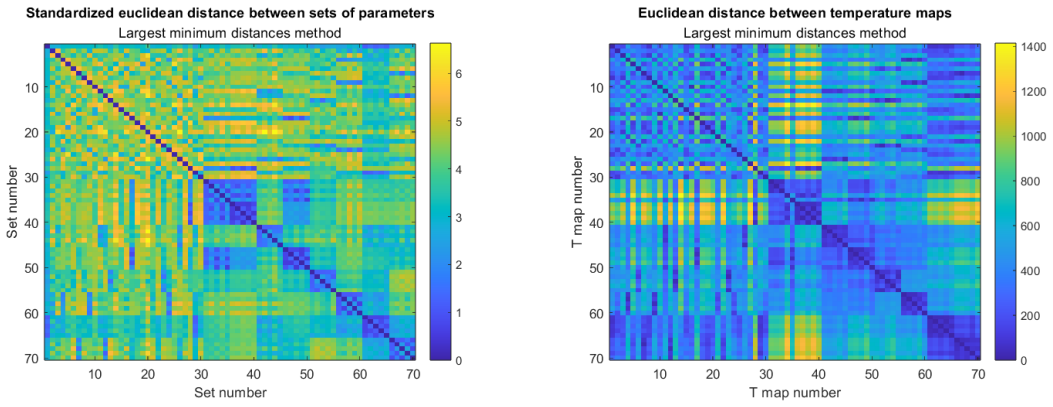

(a) (b)

Figure 4.15: Standardized euclidean distance [−] between sets of parameters (a) obtained with LMD, n = 1, d = 0.1, k = 5 and euclidean distance [$°C$] between their respective temperature maps (b).

The parameters found with this method, in general, are more broadly placed with respect to MSD.

Example: LMD n=5, d = 0.5, k = 8

In this second example, only one iteration was necessary, as the optimization parameters dictated that 40 new maps were created at once. The higher margin d allows for a larger exploration of the parameter space, as evident in Figure 4.17

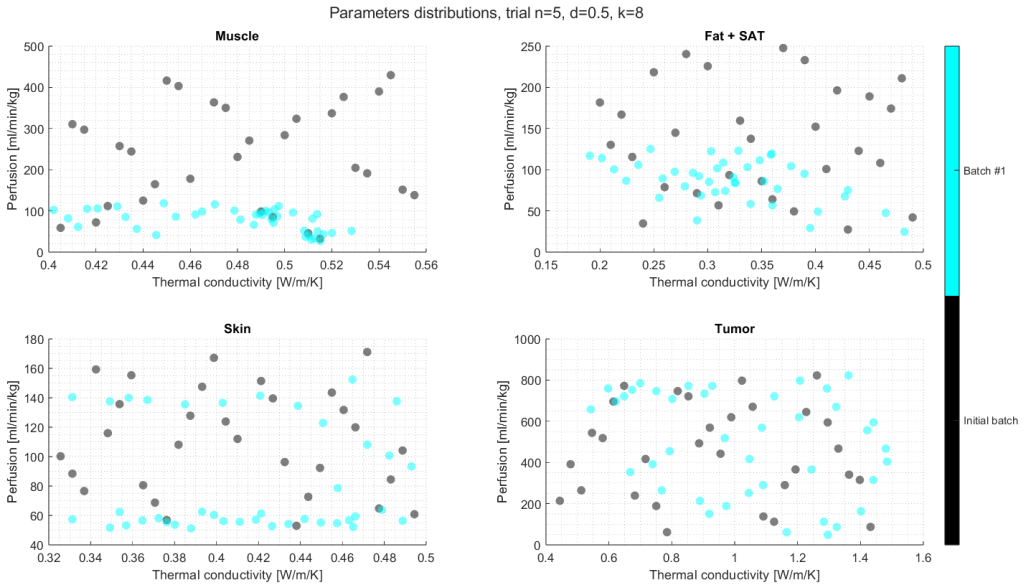

Figure 4.16: Final parameter distribution for the LMD basis created with n = 5, d = 0.5 and k = 8

The broader exploration makes this method similar to the plain Sobol, as Figure 4.2.2 confirms. The magnitude of the temperature distances is on the lower side with respect to the other methods. The big blue squared area in the lower-right part of the parameter distance plot simply indicates a superimposition of two bounding hyperspaces.

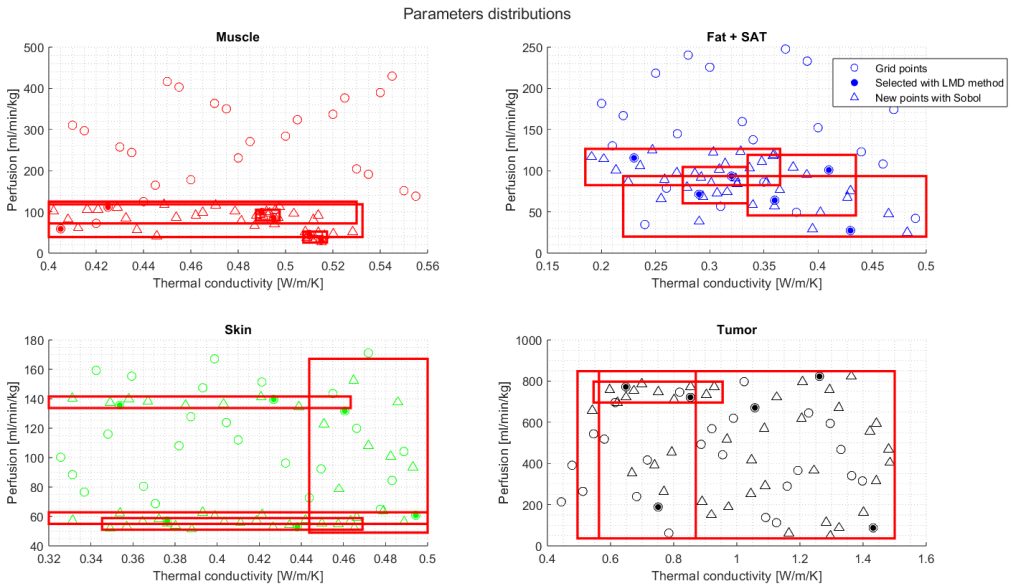

Figure 4.17: Bounding boxes created during one of the iterations with LMD, n = 5, d = 0.5 and k = 8

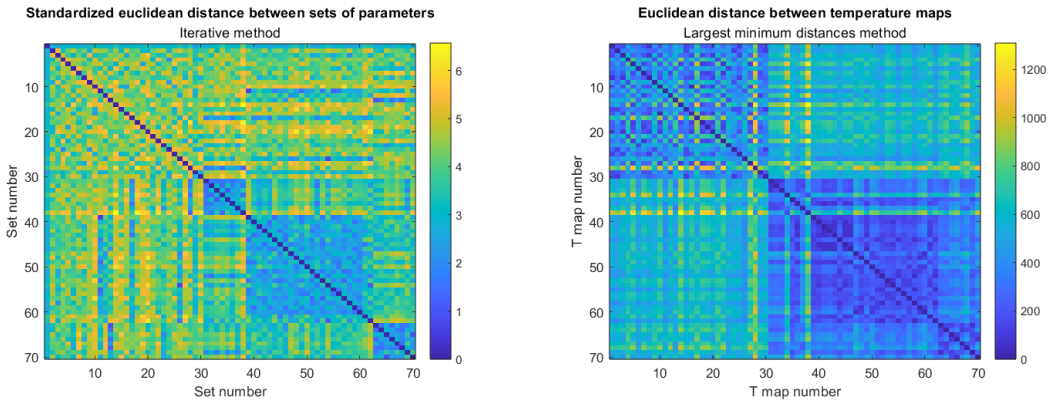

(a) (b)

Figure 4.18: Standardized euclidean distance [−] between sets of parameters (a) obtained with LMD, n = 5, d = 0.5, k = 8 and euclidean distance [°C] between their respective temperature maps (b).

4.2.3 Maximum Error Leave-One-Out method

The MELOO method identifies parameter sets associated with the highest reconstruction errors in the temperature space. The method employs a leave-one-out approach: each basis temperature map is considered as a target, one at a time, the reconstruction is attempted and the error is computed. A piece of the used code is shown in 4.5. The n maps with the highest error are then used as centers for as many bounding boxes (always within the boundaries determined by the literature). The idea is that including the neighbors of the maps that suffer from a bad reconstruction, the latter will improve.

Listing 4.5: MELOO initial selection of maps

```
% Reconstruction error analysis
for target_idx = 1:numtmaps
    f = Phi(:, target_idx);
    basis_idx = setdiff(1:numtmaps, target_idx);

    % No Noise Case
    [err_0N(:, target_idx),~] = ...
        ...Inversions(Inv_Case,zeros(length(ind_Cath),
           1),...
        ...ind_Cath,ind_ROI,Phi(:, basis_idx),f,numel(
           basis_idx));
end

% find the indexes of the tmaps with the
% largest 95th percentile error
MaxError = prctile(err_0N, 95, 1);
[~, ind_ME] = sort(MaxError, 'descend');
i0(1,:) = ind_ME(1:n);
```

Example: MELOO n=1, d = 0.1, k = 8

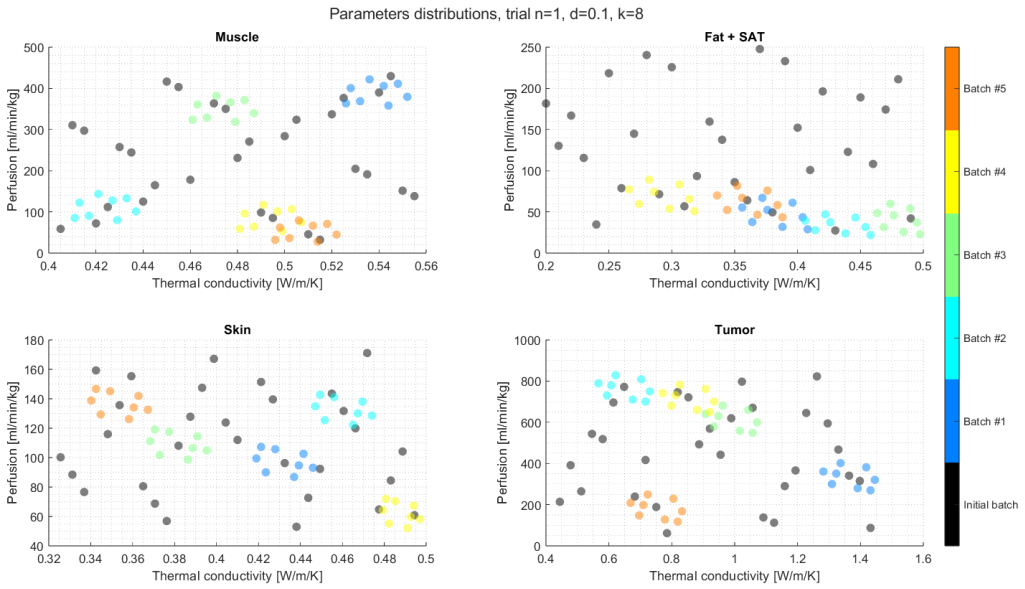

Figure 4.19: Final parameter distribution for the MELOO basis created with n=1, d = 0.1, k = 8

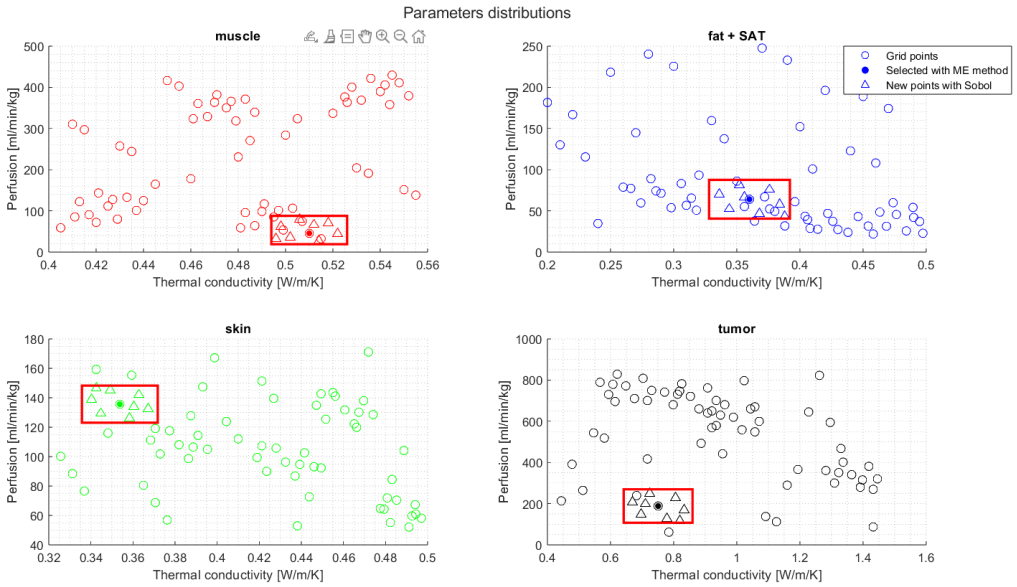

Figure 4.20: Bounding boxes created during one of the iterations with MELOO, n=1, d = 0.1, k = 8

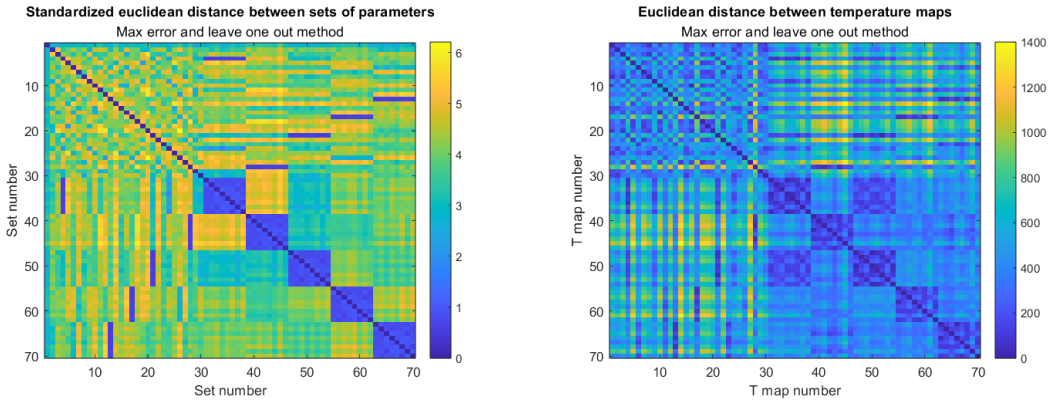

(a) (b)

Figure 4.21: Standardized euclidean distance [−] between sets of parameters (a) obtained with MELOO, n=1, d = 0.1, k = 8 and euclidean distance [$°C$] between their respective temperature maps (b).

Example: MELOO n=1, d = 0.5, k = 5

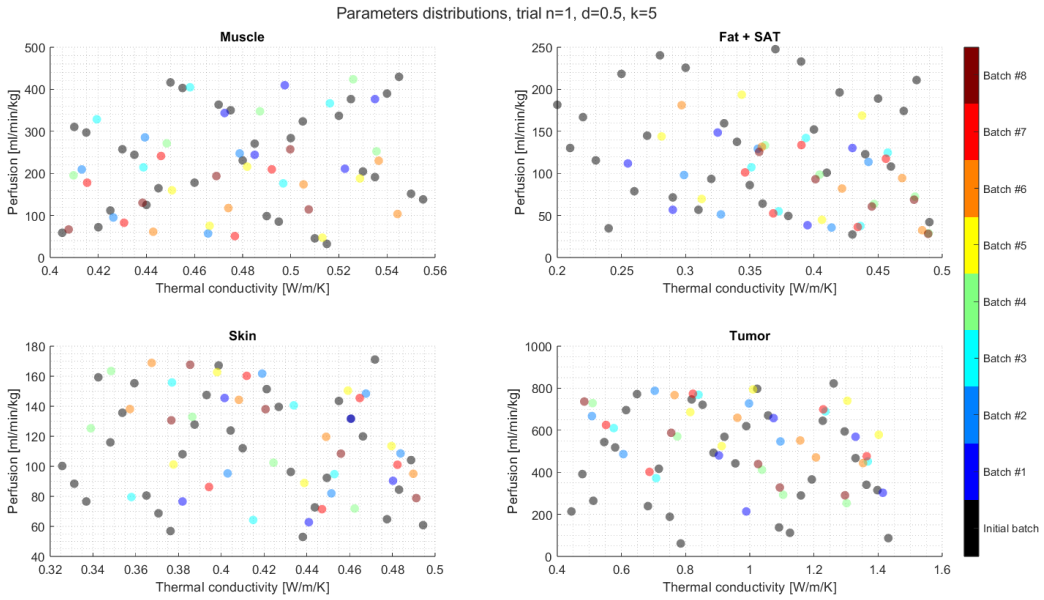

Figure 4.22: Final parameter distribution for the MELOO basis created with n = 1, d = 0.5 and k = 5

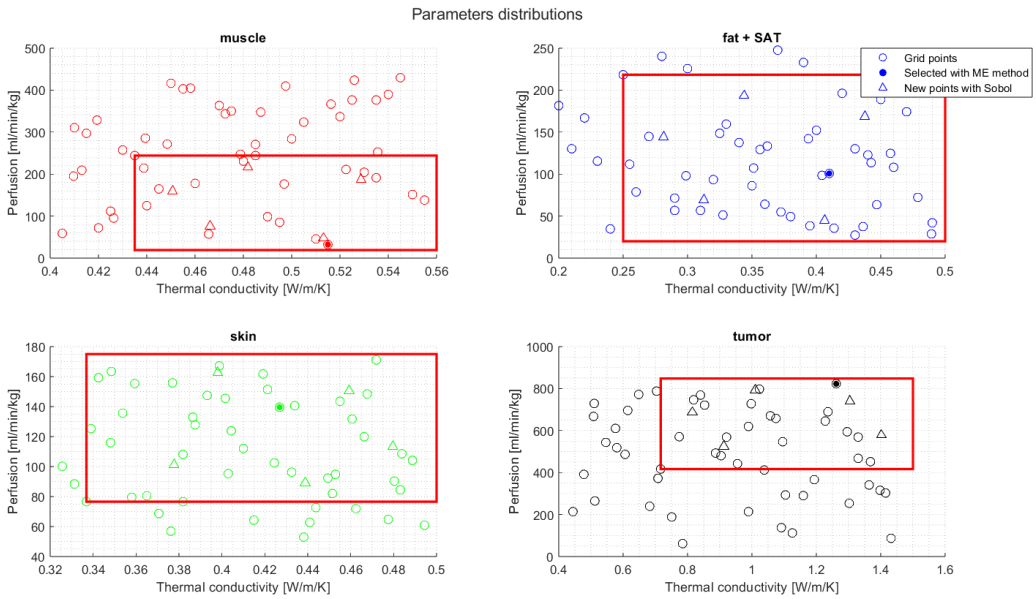

Figure 4.23: Bounding boxes created during one of the iterations with n=1, d = 0.5, k = 5

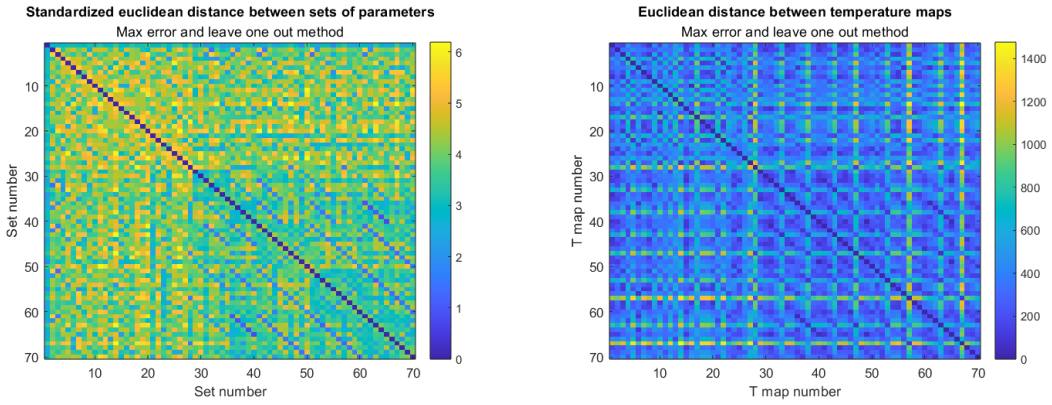

(a) (b)

Figure 4.24: Standardized euclidean distance $[-]$ between sets of parameters (a) obtained with MELOO, n = 1, d = 0.5, k = 8 and euclidean distance $[°C]$ between their respective temperature maps (b).

The peculiar distance distribution observable in Figure 4.2.3 indicates that within each batch the parameters and the temperature maps are quite different, while between different batches some parameters and maps have some similarities.

4.3 Accuracy analysis

4.3.1 Study on 500 Sobol targets

A Φ_t with 500 target maps was used to provide a statistically strong testbed and evaluate the efficacy of the optimization with respect to the uniform basis. Six metrics were used:

- χ_{95}, across 500 noiseless targets and 100000 noisy targets (each Φ_t target being added 200 realizations of Gaussian noise on the measurement points), similarly to 3.3.
- ΔT_{50}, ΔT_{90}, maximum error ($Max\ Error$), 99.9th percentile of error, 95th quantile and 95th superquantile of error across the 100000 noisy targets.

The superquantile measure, also known as the *conditional value at risk (CVaR)* is a risk measure that extends the concept of quantiles (or *value at risk*, VaR). For a given probability level $\alpha \in (0,1)$, the superquantile of a random variable X, denoted as $\mathrm{SQ}_\alpha(X)$, is defined as:

$$\mathrm{SQ}_\alpha(X) = \mathbb{E}[X \mid X \geq Q_\alpha(X)] \tag{4.2}$$

where $Q_\alpha(X)$ is the *quantile function* which satisfies:

$$Q_\alpha(X) = \inf\{x \in \mathbb{R} \mid P(X \leq x) \geq \alpha\}. \tag{4.3}$$

In other words, the superquantile at level α is the expected value of X given that X exceeds the quantile $Q_\alpha(X)$. In Matlab, the 95th superquantile of the error for the j-th method is calculated as in 4.6:

Listing 4.6: superquantile formula in Matlab

```
error95_quantile(j) = quantile(error_samples(:,j), 0.95);
error95_superquantile(j) = error95_quantile(j) + 1/(1-0.95)
    * mean((max(erro_samples(:,j) - error95_quantile(j), 0)))
    ;
```

where:

- error95_quantile(j) calculates the 95th quantile of the error.
- error_samples(:, j) represents the reconstruction error data for the j -th method.
- max(error95_samples(:, j) − error95_quantile(j), 0) extracts the values that exceed the quantile threshold (tail losses).
- The mean($\cdot$) computes the expectation of the tail losses, which is multiplied by the scaling factor $1/(1 - 0.95) = 20$.

This method provides a more robust risk assessment compared to the quantile (VaR) by considering the magnitude of extreme losses rather than just the threshold.

The number of catheter points was still 20 and *LSQLIN constraints* was used due to the conclusions from the S-parameters experiment (in the y-direction to maintain consistency with previous studies that adopted this orientation).

Table 4.1: $\mathcal{X}_{95}$ [$^{\circ}C$] without any noise added

Optimization parameters	**Method**			
	LMD	MSD	MELOO	Sobol
n=1, d=0.1, k=5	1.2563	1.2286	1.2500	1.0750
n=1, d=0.1, k=8	1.2400	1.2143	1.2389	
n=1, d=0.5, k=5	1.2333	1.2389	1.1667	
n=1, d=0.5, k=8	1.3000	1.2700	1.1250	
n=5, d=0.1, k=5	1.2333	1.2500	1.2400	
n=5, d=0.1, k=8	1.2643	1.2857	1.1625	
n=5, d=0.5, k=5	1.2300	1.2286	1.1286	
n=5, d=0.5, k=8	1.2429	1.2917	1.1000	

Table 4.2: $\mathcal{X}_{95}$ [$^{\circ}C$] with Gaussian noise added to the 20 catheter measurements.

Optimization parameters	**Method**			
	LMD	MSD	MELOO	Sobol
n=1, d=0.1, k=5	1.2408	1.2394	1.2468	1.1180
n=1, d=0.1, k=8	1.2600	1.2581	1.2613	
n=1, d=0.5, k=5	1.2477	1.2641	1.2216	
n=1, d=0.5, k=8	1.3232	1.2932	1.1909	
n=5, d=0.1, k=5	1.2407	1.2441	1.2392	
n=5, d=0.1, k=8	1.2884	1.3016	1.2251	
n=5, d=0.5, k=5	1.2487	1.2369	1.1597	
n=5, d=0.5, k=8	1.2556	1.3362	1.2081	

In the noiseless scenario (Table 4.1), the baseline Sobol method yielded a χ_{95} of 1.0750 °C, serving as reference for comparison. Among the optimized methods, the MELOO approach achieved the best performance, with a χ_{95} of 1.1000 °C in its best configuration (n=5, d=0.5, k=8). The MSD method followed with a χ_{95} of 1.2143 °C in its best configuration (n=1, d=0.1, k=8), while the LMD method yielded a χ_{95} of 1.2300 °C with n=5, d=0.5, k=5.

Under noisy conditions (Table 4.2), the baseline Sobol method exhibited a χ_{95} of 1.1180 °C. The optimized methods maintained a similar ranking as in the noiseless

case, with MELOO again achieving the lowest value at 1.1597 °C, followed by MSD at 1.2369 °C and LMD at 1.2407 °C. Although all methods suffered a slight increase in error thresholds under noise, as expected, Sobol remained the best method. The results indicate that no optimized method consistently outperforms the others across all conditions, as their performance varied with different parameter configurations.

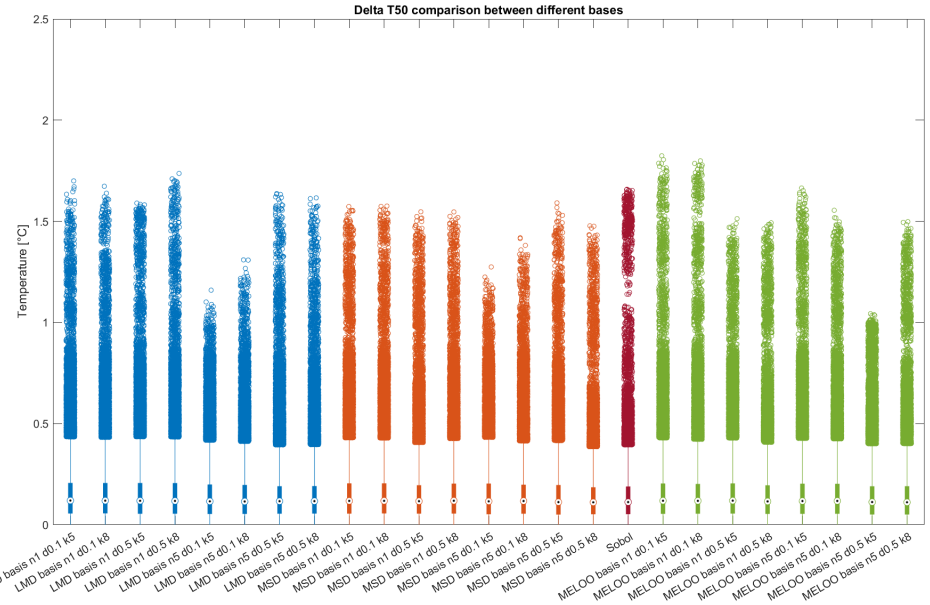

Figure 4.25: Boxplot of ΔT_{50} (absolute difference between the reconstructed median temperature in the tumor and the actual one) between the different basis

The analysis on $\Delta T50$ (Figure 4.25), $\Delta T90$ (Figure 4.26), *Max Error* (Figure 4.27) and the 99.9*th* percentile of error (Figure 4.28) could not bring to any particular conclusion. The median for all the considered realizations, which is identified by the circle with a dot at its center within the bold vertical bar, is slightly lower with Sobol for all four metrics (0.1253 °C, 0.1261 °C, 0.9099 °C, 0.8565 °C, respectively) . This indicates that there is no measurable improvement of these metrics after the optimization of the bases. The temperature reconstruction in the tumor, which accounts for 0.016% of the total volume, showed good, but still not acceptable values of accuracy, with a $\Delta T50$ and $\Delta T90$ below 0.3 °C for more than 75% of the realizations.

Figure 4.29 indicates that Sobol has the better 95th quantile (1.15 °C) and that MELOO falls short from it (1.25 °C). There seems also to be a tendency of this metric to be higher when k = 8, in particular for the LM and MSD methods, suggesting a slightly larger error when considering many new points in the region

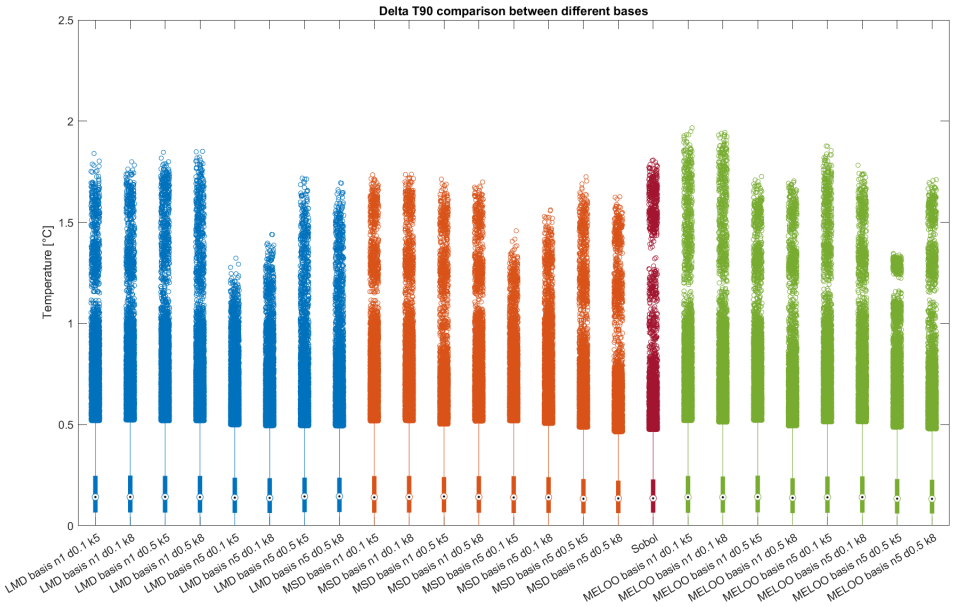

Figure 4.26: Boxplot of ΔT_{90} (absolute difference between the reconstructed 90th percentile of temperature in the tumor and the actual one) between the different basis

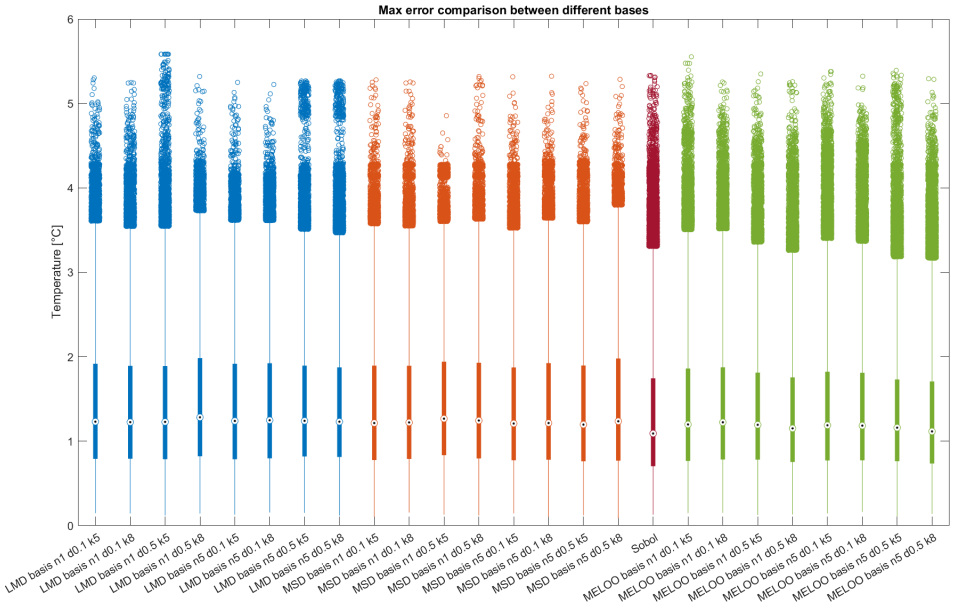

Figure 4.27: Boxplot of *Max Error* associated to the different bases

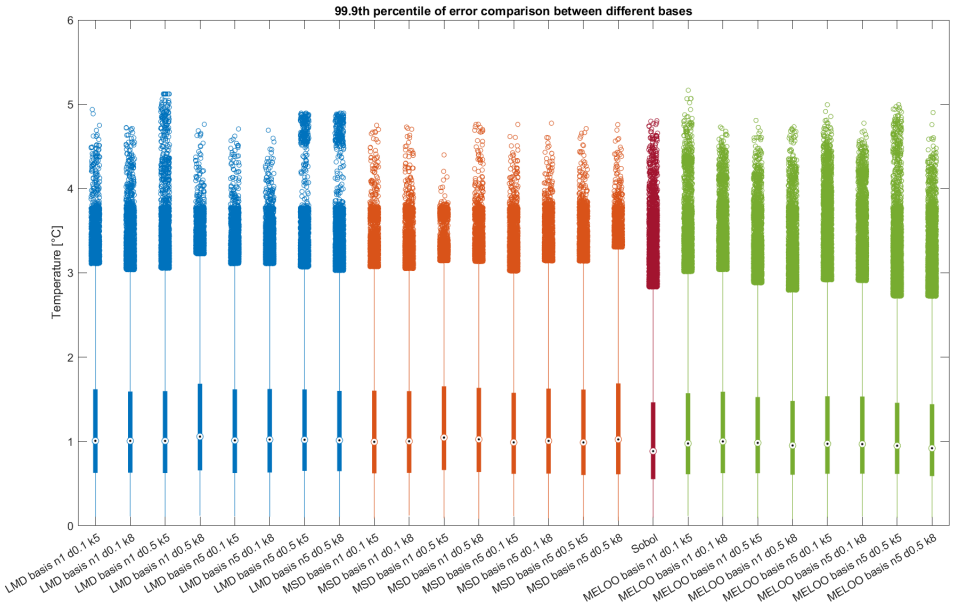

Figure 4.28: Boxplot of 99.9*th* percentile of error [°C]associated to the different bases

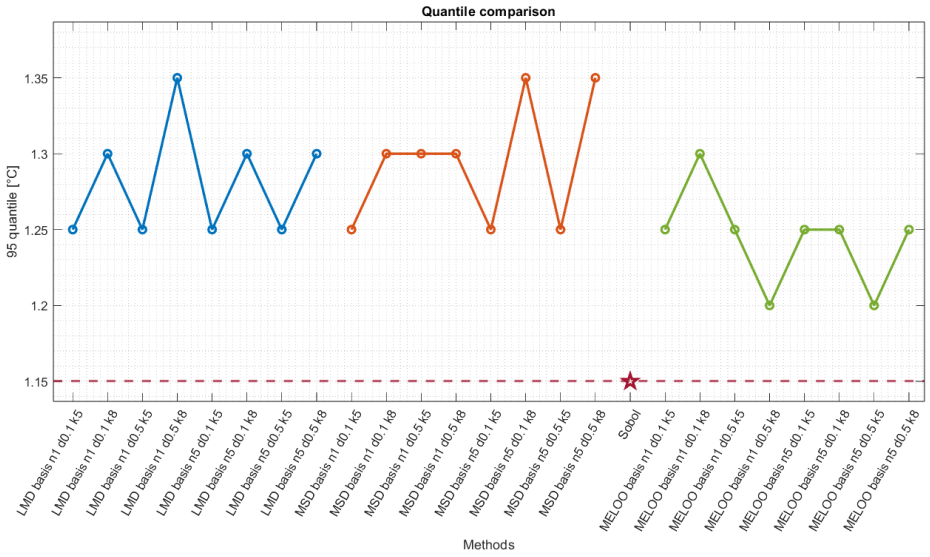

Figure 4.29: 95*th* quantile of error associated to the different bases

selected by the algorithm. Finally, Figure 4.29 indicates that MSD has overall better 95th superquantiles (min 1.449 °C) with respect to Sobol (1.466 °C). MELOO performs the worst, with a minimum 95th superquantile of 1.512 °C. Unfortunately,

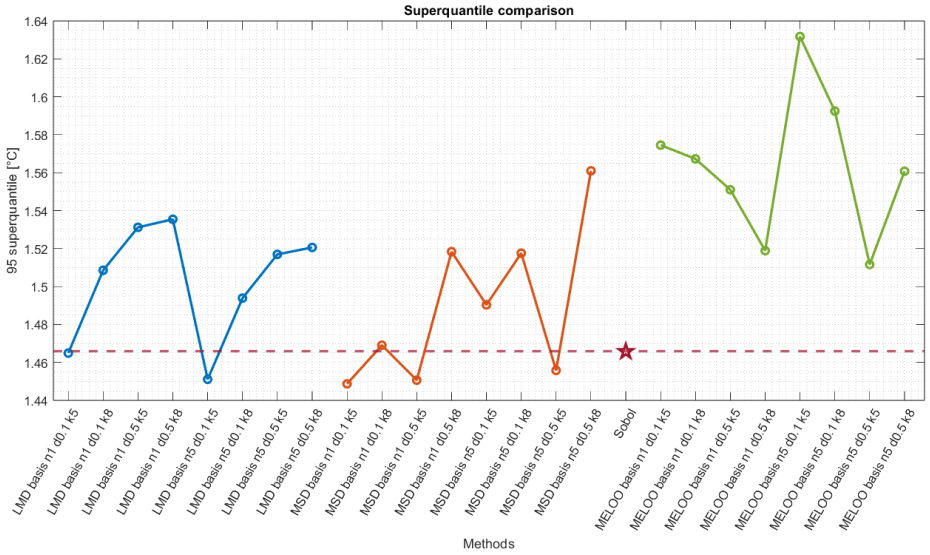

Figure 4.30: $95th$ superquantile of error [°C] associated to the different bases

a 0.017 °C difference cannot be accounted as a significant improvement, but the results suggest that MSD could be better than MELOO at mitigating extreme errors without increasing their occurrence.

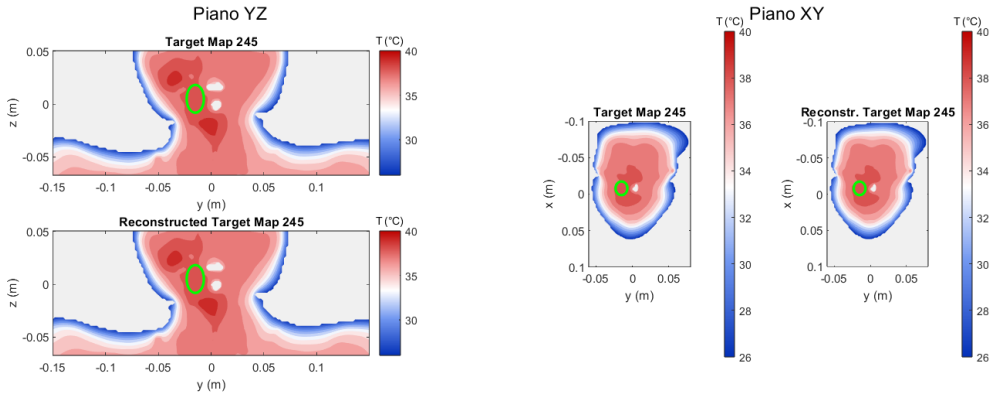

(a) (b)

Figure 4.31: Example of good temperature reconstruction: comparison of true vs. reconstructed target map n.245 on the YZ plane, at x coordinate of the tumor center (a) and on the XY plane, at z coordinate of the tumor center (b).

Figure 4.3.1 shows an example of good temperature prediction obtained with one of the optimized methods. In contrast, 4.3.1 shows one of the worst reconstructed temperature distributions, where the temperature underestimate is evident both in

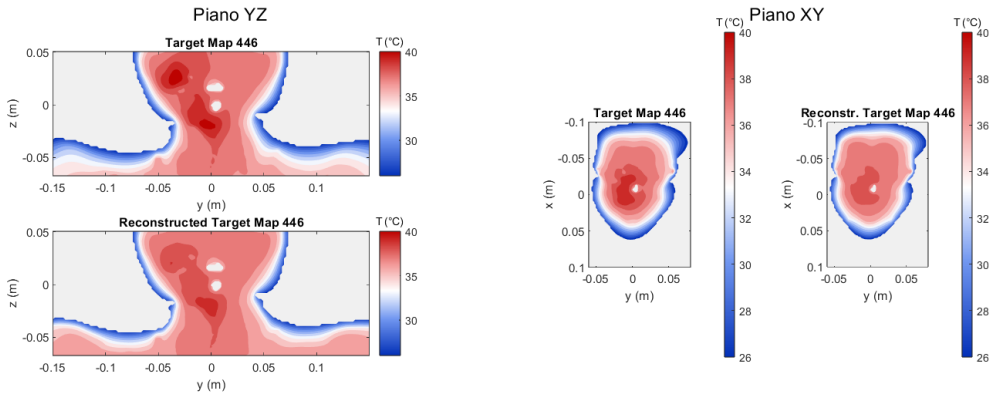

(a) (b)

Figure 4.32: Example of bad temperature reconstruction: comparison of true vs. reconstructed target map n.446 on the YZ plane, at x coordinate of the tumor center (a) and on the XY plane, at z coordinate of the tumor center (b).

the YZ and in the XY plane.

4.3.2 Study on 256 extreme targets

The last study was carried out using all possible combinations of parameters at the vertices of the 8-D parameter space, with the aim of quantifying the quality of reconstruction for the most extreme cases (the ones that differ the most from the baseline values). The number of vertices of this space is equal to $2^8 = 256$, therefore, 256 targets were considered.

Listing 4.7: sampling of the most extreme parameter sets

```
function MGrid = MultiGrid_extreme(filepath,param,
    tissue)
table = cell(1,numel(param));
for i = 1:numel(param)
    table{i} = xlsread(filepath,param(i),'A1:D5');
    table{i} = table{i}(tissue,:);
end
ranges = cell(numel(tissue),numel(param));
for i = 1:numel(tissue)
    for j = 1:numel(param)
        ranges{i,j} = [table{j}(i,2),table{j}(i,3)];
    end
end
output = cell(1,numel(param)*numel(tissue));
[output{:}] = ndgrid(ranges{:});
results = [];
for i = 1:length(output)
    results = [results output{1,i}(:)];
end

MGrid = results;
end
```

The results were much worse than the ones obtained considering the entire volume; however, in relative terms, the optimized methods performed better than Sobol, lowering the χ_{95} from 3.33 °C to 2.89 °C (MSD, n=1, d=0.5, k=8,) in the noiseless case (Table 4.3). The reduction of approximately 0.44 °C in the error threshold indicates that the MSD method can contribute to a more accurate reconstruction in these challenging conditions. The same thing can be said for the LMD method, which achieved a χ_{95} of 2.94 °C under the same configuration. The MELOO method provided mixed results. In the best-case configuration, it produced a χ_{95} of 2.97 °C, which is very close to MSD and LMD, but in half of the cases it was higher than Sobol. It appears that this method lacks the generalization capability provided by the other sampling strategies.

Table 4.3: $\mathcal{X}_{95}$ [$^{\circ}C$] without any noise added

Optimization parameters	**Method**			
	LMD	MSD	MELOO	Sobol
n=1, d=0.1, k=5	3.0140	2.9900	3.8866	3.3300
n=1, d=0.1, k=8	2.9775	2.9025	2.9700	
n=1, d=0.5, k=5	3.0887	3.0275	3.0600	
n=1, d=0.5, k=8	2.9366	2.8900	3.0720	
n=5, d=0.1, k=5	3.0844	3.1020	3.2100	
n=5, d=0.1, k=8	2.9650	2.9514	3.8400	
n=5, d=0.5, k=5	3.0866	3.0400	3.4800	
n=5, d=0.5, k=8	3.0866	2.860	3.3740	

Table 4.4: $\mathcal{X}_{95}$ [$^{\circ}C$] with Gaussian noise added to the 20 catheter measurements.

Optimization parameters	**Method**			
	LMD	MSD	MELOO	Sobol
n=1, d=0.1, k=5	3.0148	2.9833	3.9403	3.3937
n=1, d=0.1, k=8	2.9467	2.8578	3.0923	
n=1, d=0.5, k=5	3.0908	2.9946	3.0850	
n=1, d=0.5, k=8	2.8256	2.8200	3.0336	
n=5, d=0.1, k=5	3.0716	3.0850	3.3403	
n=5, d=0.1, k=8	2.8603	2.8393	3.9878	
n=5, d=0.5, k=5	3.0675	3.0547	3.5111	
n=5, d=0.5, k=8	3.0754	2.7652	3.4811	

Under noisy conditions (Table 4.4), the Sobol method exhibited a χ_{95} of 3.39 °C, while the MSD method maintained its lead, achieving a χ_{95} of 2.82 °C, showing a strong resilience to noise. This indicates that the maps selected through the MSD strategy not only span a broad and diverse range of the parameter space but also provide stable reconstructions. The LMD method also demonstrated robustness, with a χ_{95} of 2.83 °C, closely following MSD. The MELOO method, while still an improvement over Sobol, showed a higher χ_{95} of 3.03 °C in the noisy scenario.

In addition, in this case, the analysis of $\Delta T50$ (Figure 4.33), $\Delta T90$ (Figure 4.34), $Max\ Error$ (Figure 4.35) and the $99.9th$ percentile of error (Figure 4.36) could not reach any significant conclusion. However, the median for all the considered realizations tended to be the highest with Sobol for $\Delta T50$ and $\Delta T90$ (0.328 °C, 0.355 °C, respectively). MELOO slightly outperformed Sobol with a lower $Max\ Error$ (1.878 °C vs. 2.095 °C); similar results are obtained for the $99.9th$ percentile of error.

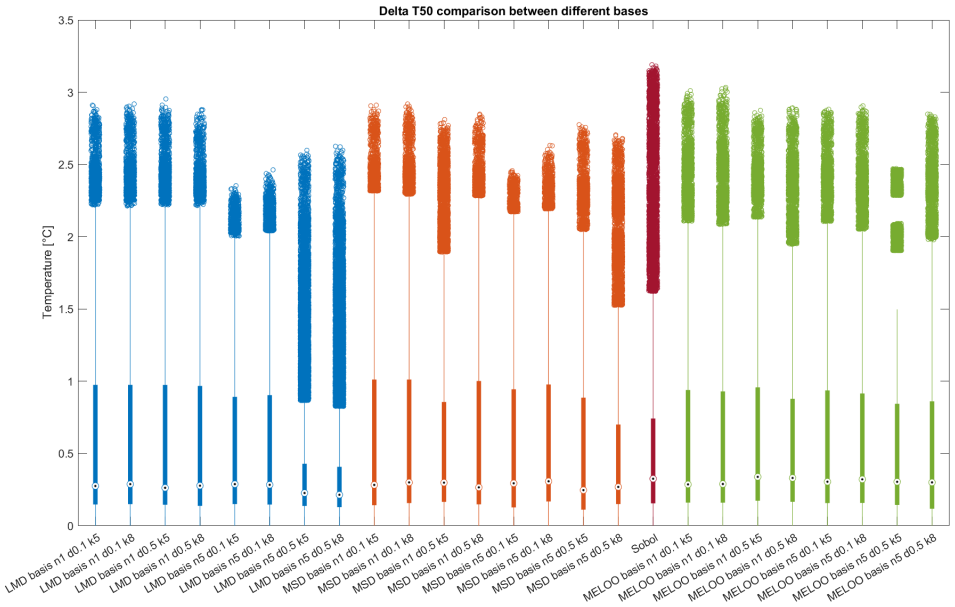

Figure 4.33: ΔT_{50} (absolute difference between the reconstructed median temperature in the tumor and the actual one) between the different basis

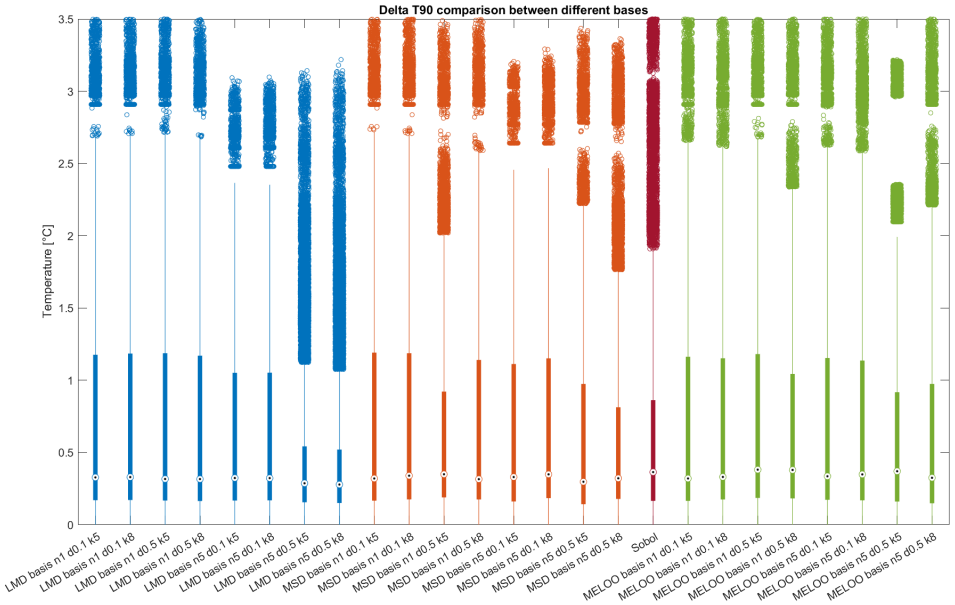

Figure 4.34: ΔT_{90} (absolute difference between the reconstructed 90th percentile of temperature in the tumor and the actual one) between the different basis

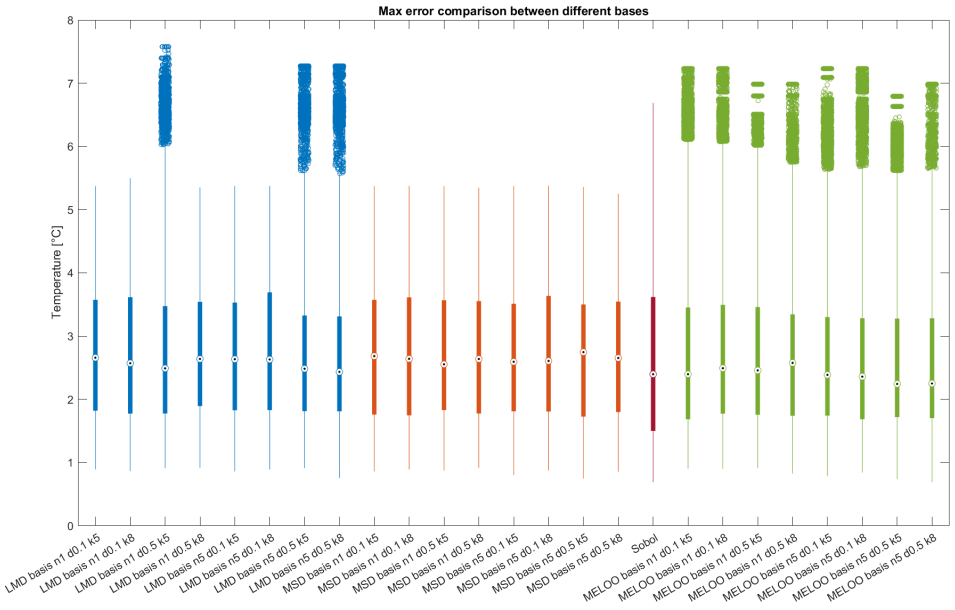

Figure 4.35: *Max Error* associated to the different bases

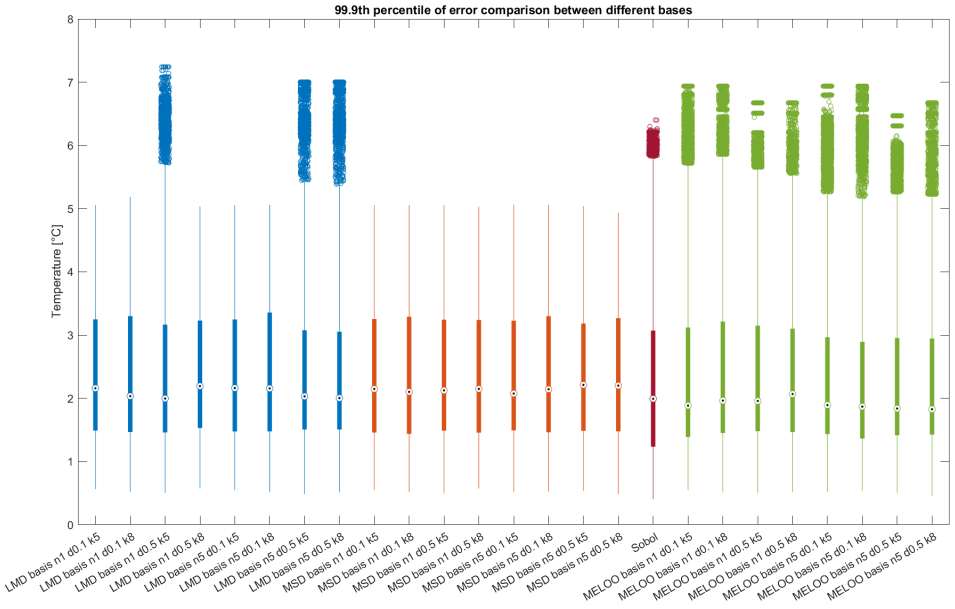

Figure 4.36: 99.9*th* percentile of error associated to the different bases

Finally, Figure 4.29 indicates that in these extreme cases, MSD has relatively better 95th superquantiles (min 2.981 °C) with respect to Sobol (3.927 °C). MELOO performs the worst overall, with a minimum 95th superquantile of 3.58 °C. LMD

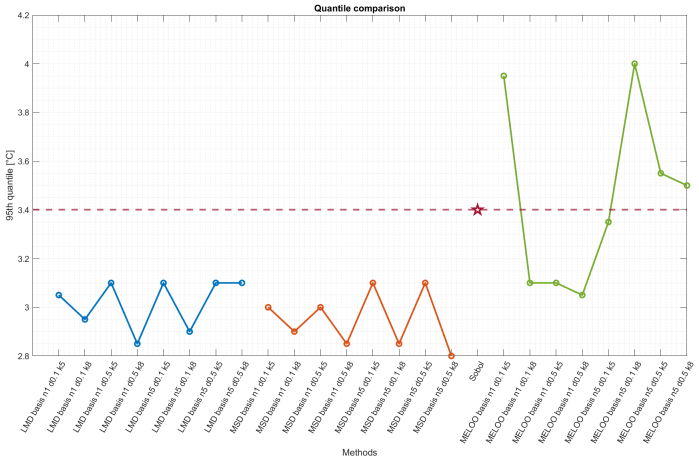

Figure 4.37: 95th quantile of error associated to the different bases

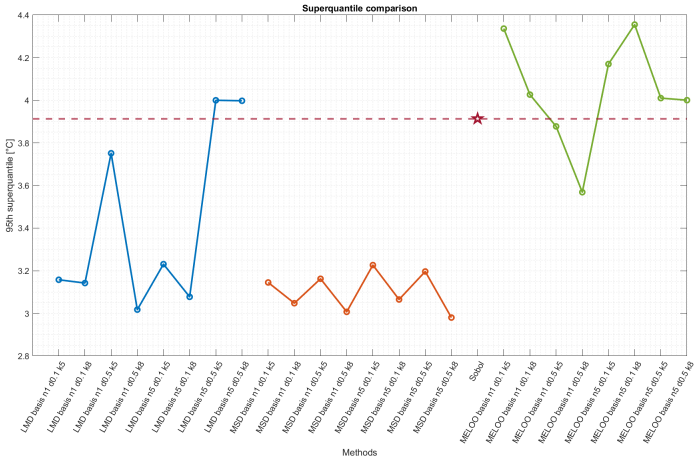

Figure 4.38: 95th superquantile of error associated to the different bases

has also several configurations below the Sobol value. These results suggest that the optimizations based on the distance generally improves the reconstruction in cases where the patient has tissue properties that diverge significantly from the baseline values. Unfortunately, these high errors would still limit, if not deny, the application of therapy in such cases.

4.4 Preliminary studies

This section describes some of the discarded ideas, as they can provide some interesting insights for future research.

The MSD was initially created similarly to a Maximum Distances (MD) method, which:

1. Selected the temperature maps with the singular highest distances ($> 75th$ percentile)
2. Applied hierarchical clustering in the related points of the parameter space through the Matlab function `clusterdata`, with the input "distance" set to "standardized euclidean" and the input "linkage" set to "complete" (farthest distance between clusters); the number of clusters was automatically set by imposing a 10% threshold on the Within-Cluster Sum of Squares (WCSS). This was needed to avoid the superimposition of too many bounding boxes, creating just the necessary amount.
3. created the bounding box around the centroids of the clusters.
4. Produced 25 additional sets of parameters and related temperature maps, with Sobol. The new points were split according to the number of clusters (e.g. if there were 3 clusters, the number of new points in each bounding box was 8, 8, 9, respectively)
5. Repeat for one and last iteration, considering only the 25 maps just created.

The idea was to exacerbate the mentioned condition (MD or MSD) on the temperature distance, in order to have a basis which contained some of the "worse cases". However, it ignored the relationships between the three batches, excluding some potential information. For this reason and because of its too many arbitrary variables, this approach was excluded, preserving only the idea of the bounding boxes. The last 10 from the third batch, which represented the "most distinctive" maps, were used as targets instead of being part of Φ. Together with them, 10 additional targets were created with Sobol and the 20 resulting maps were used to evaluate some early reconstruction results.

The LMD also had a preliminary version, "LMD with mean", where Φ was built in 40 iterations (starting from 30 Sobol maps) structured as:

1. evaluate the minimum distances in the temperature space, excluding the diagonal
2. find the index $i0$ of the map with the largest minimum distance (this isolates the first map of the pair)
3. find the index $i1$ of the closest temperature map (this isolates the second one)

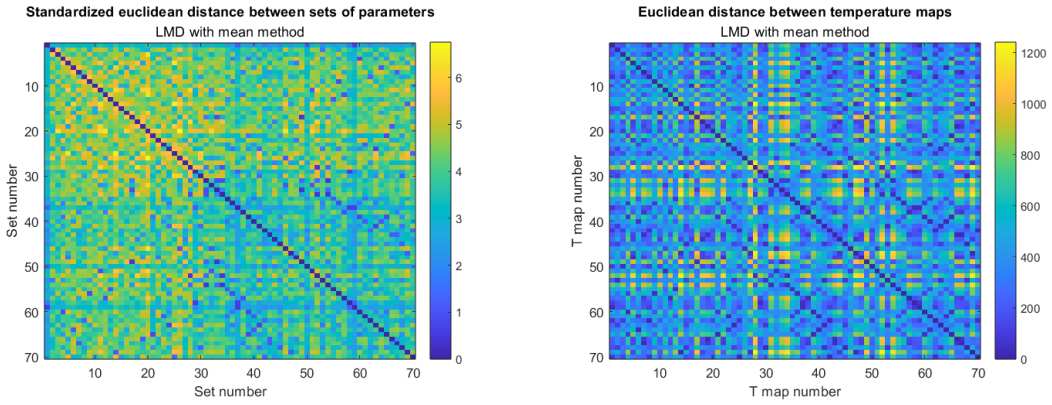

(a) (b)

Figure 4.39: Standardized euclidean distance [−] between sets of parameters (a) obtained with LMD (with mean) and euclidean distance [°C] between their respective temperature maps (b).

4. evaluate the mean between the set of parameters ξ_{i0} and the set of parameters ξ_{i1}, for each tissue.
5. perform the thermal simulation using the new set of k and w
6. repeat until reaching 80 temperature maps. The last 10 were used as targets.

It might be interesting to note that this method also showed a distance uniformity similar to that observed with Sobol, as shown in Figure 4.4 (b).

In summary, some reconstructions were performed with the following:

- MD basis vs. Sobol basis using 10 MD and 10 Sobol targets
- MD basis vs. Sobol basis with 10 MSD and 10 Sobol targets
- LMD with mean basis vs. Sobol basis with 10 LMD and 10 Sobol targets

The median of the 5th, 25th, 50th, 75th, and 95th percentiles of error across the target maps and the realizations are shown in Figure 4.40

As can be observed in Figure 4.41, the Sobol basis poorly reconstructed all the targets coming from the last batch of MD and more than half of those from the last batch of MSD (previous version), confirming the negative effects of the magnitude of the distance on the inversion algorithms. As for the MD basis, despite its good early performance, it was discarded for its poor explainability and for the fact that it tended to always select the same maps when increasing the number of iterations. The LMD with mean approach was later adapted to become the one previously described because the linear combination of the two sets, instead of a convex one,

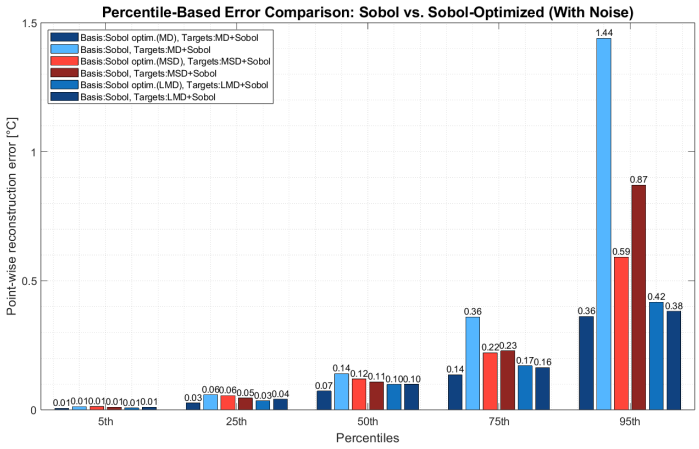

Figure 4.40: 5th, 25th, 50th, 75th and 95th percentiles of error during reconstruction with few, mixed targets.

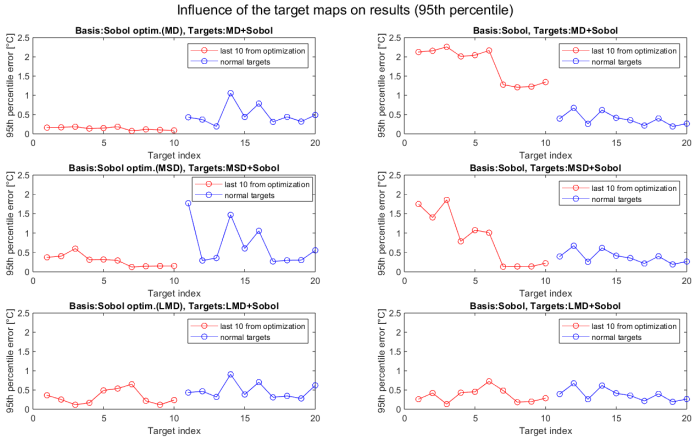

Figure 4.41: 95th percentile of error evaluated on each target map. Red dots represent the performance on the last 10 maps created with the optimization, blu dots the the performance on 10 uniformly distributed targets

ultimately produced a temperature-distance matrix with lower values.

Discussion

This thesis focused on improving temperature predictions in microwave hyperthermia for head and neck cancer treatments by combining electromagnetic and thermal simulations with enhanced reconstruction strategies. Traditionally, thermometry catheters provide only a small number of invasive temperature readings, and baseline tissue parameters often fail to capture their natural variability between patients. To address this, a detailed digital phantom was used, and different tissue properties were imposed by sampling the parameter space, thereby generating a library of simulated temperature maps.

Inversion techniques using catheter data and additional non-invasive antenna reflection coefficients were used to refine temperature estimates, with little success. As explained in Chapter 3, the impact of the S parameters on reconstruction quality varies between the different metrics, showing negligible influence on χ_{95} and some positive effects on ΔT and ΔT_{50}, particularly in the presence of noise. *LSQLIN constraints* provide the best performance in the presence of noise, which is arguably the most realistic scenario. The choice of the best method should not strictly depend on its performance in the two directions of the catheter, as they were arbitrarily chosen. In a clinical setting, the catheter insertion path must be defined in order to minimize damage to the specific structures of the head and neck of the patient, so the actual positioning may differ significantly from the configurations analyzed in this study. Comparison with χ_{95} obtained using the entire ROI rather than catheter measurements reinforces the idea that χ_{95} is mainly determined by temperature-related information rather than additional EM information. The main reason could lie in the fact that the S parameters are one to two orders of magnitude smaller than the temperatures, providing little to no additional information in the reconstruction. Another explanation could be that their sensitivity to the variation of dielectric parameters is too small to be used on a par with that of an actual sensor. A future development could involve a normalization phase that better exploits the magnitude and/or dynamic of the reflection coefficient instead of using their raw values.

Finally, to improve the performances obtained with a plain Sobol basis, it was

assumed that uniform sampling probably overlooked the complexity of the tissues' thermal response to MW irradiation. Therefore, some iterative targeted sampling approaches were designed to build an optimized Φ that could keep up with some challenging temperature maps and simultaneously avoid including similar maps inside it. The results probably left us with more questions than answers. It was hypothesized that the implementation of strict metrics (e.g. χ_{95}) was downplaying the effects of optimization, so other estimators were considered. Unfortunately, the analysis still lacked strong results, either positive or negative, which could have guided the investigation toward a specific method. Further analysis of the error associated with each target map revealed that some targets were still badly reconstructed even when their parameters were close to large clusters of parameters whose maps were used in the basis. This suggests that the reconstruction performance, even in the optimized cases, mostly depends on the overall distribution of the parameters rather than on some local "enhancements". However, other attempts with different values of n, d, and k could be attempted; the MD method could also benefit from a rework and be evaluated. Finally, since this work basically produced a comprehensive dataset of unique parameter combinations and their associated temperature maps (1530 including the 25 bases and the target maps), the implementation of machine learning to find the best parameter configuration to obtain the best reconstruction is surely appealing. Deep learning could also be implemented, as it appears that features that link the parameter space to the temperature space are not as straightforward as we thought and may need some more complex elaboration to be found.

Appendix A

Sim4Life

Sim4Life, product by ZMT Zurich MedTech, is a multiphysics simulation platform for computational life scientists. It combines computable human phantoms with powerful physics solvers and advanced tissue models. The software directly analyzes biological phenomena and complex technical devices in a validated biological and anatomical environment. The software phantoms subsequently provide a realistic biological environment to conduct fundamental studies to test the effectiveness and safety of medical devices and treatments, and to supplement clinical trials [40]. The Electromagnetic Full Wave Solvers (P-EM-FDTD) enable accelerated full-wave, large-scale EM modeling (billion voxels) with Yee discretization on geometrically adaptive, inhomogeneous, rectilinear meshes with conformal sub-cell correction and thin layer models. These solvers, which are the most frequently applied in near-field dosimetry, have been extensively validated and documented according to the IEEE / IEC 62704-1 standard, as well as by comparisons with measured data [40].

A.1 Discretization of Maxwells Equations

The Finite-Difference Time-Domain method (FDTD) proposed by Yee in 1966 is a direct solution of Maxwells curl equations in the time domain. The electric (E-field) and magnetic (H-field) components are allocated in space on a staggered mesh of a Cartesian coordinate system. The E and H field components are updated in a leap-frog scheme according to the finite-difference form of the curl surrounding the component. The transient fields can be calculated when the initial field, boundary, and source conditions are known.

Maxwells curl equations are discretized by means of a second-order finite-difference approximation both in space and in time in an equidistantly spaced mesh. The first

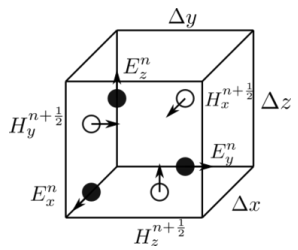

Figure A.1: 3D Yee cell showing the E- and H-field components in the staggered grid.

partial space and time derivatives lead to:

$$\frac{\partial F(i,j,k,n)}{\partial x} = \frac{F^n(i+1/2,j,k) - F^n(i-1/2,j,k)}{\Delta x} + O[(\Delta x)^2]$$
$$\frac{\partial F(i,j,k,n)}{\partial t} = \frac{F^{n+1/2}(i,j,k) - F^{n-1/2}(i,j,k)}{\Delta t} + O[(\Delta t)^2]$$

A.1.1 Numerical Stability

For the explicit finite difference scheme to yield a stable solution, the time step used for updating must be limited according to the Courant-Friedrich-Levy (CFL) criterion [41]. This is a stability condition for time discretization:

$$\Delta t \leq \frac{1}{c\sqrt{\frac{1}{(\Delta x)^2} + \frac{1}{(\Delta y)^2} + \frac{1}{(\Delta z)^2}}}$$

where Δx, Δy, and Δz are the mesh steps of a Cartesian coordinate system and c is the speed of light within the material of a cell.

Appendix B

Sobol sequence implementation

Listing B.1: loading of the tissue parameters and definition of the number of points

```
% Multi-dimensional pseudo-random Sobol grid.
% The parameters are organized in an external Excel file.


clear all
%clc

filename = 'NewParameters.xlsx';
filepath = [pwd, '\',filename];

% Type of parameters: [epsr,sigma,k,w]
param = [1,2,3,4];

% Type of tissues: [Muscle,Fat,Skin,Tumor]
tissue = [1,2,3,4];

Ns = 1000;                    % [-]  number of Sobol quasi-
    random points

MGrid = MultiGrid_Sobol(filepath,param,tissue,Ns);
save([pwd, '\MGrid.txt'], 'MGrid', '-ascii', '-tabs');
```

where:

Listing B.2: Sobol semi-random sequence

```
% Multi-dimensional pseudo-random Sobol grid
% The parameters are organized in an external Excel file.


function MGrid = MultiGrid_Sobol(filepath,param,tissue,S)

table = cell(1,numel(param));

for i = 1:numel(param)
    table{i} = xlsread(filepath,param(i),'A1:D5');
    table{i} = table{i}(tissue,:);
end

ranges = cell(numel(tissue),numel(param));

for i = 1:numel(tissue)
    for j = 1:numel(param)
        ranges{i,j} = [table{j}(i,2),table{j}(i,3)];
    end
end

%%% Quasi random Sobol sequence (green points) %%%
% creo numeri quasi casuali
q = qrandstream('sobol',numel(param)*numel(tissue),'Skip'
    ,1);

% genero numeri dal flusso di numeri casuali q anziché dal
    flusso globale
% predefinito. avrò S righe e 16 colonne
X = rand(q,S,numel(param)*numel(tissue));

% metto in colonne i minimi e i massimi, le righe sono: le
    prime 4 le epsr
% di muscle, fat, skin, tumor, poi le seconde 4 sono le
    sigma, ecc...
RF = reshape([ranges{:}],2,numel(param)*numel(tissue)).';

% ogni colonna di X viene sostituita con un valore
    semicasuale tra max e
```

```
% min del parametro del tessuto corrispondente alla riga di
    RF
for i = 1:length(RF)
    X(:,i) = RF(i,1)+range(RF(i,:)).*X(:,i);
end

MGrid = X;


end
```

Bibliography

[1] Szasz A., Szasz O., Szasz N., *Physical Background and Technical Realizations of Hyperthermia*, Madame Curie Bioscience Database, Austin (TX): Landes Bioscience; 20002013.

[2] Conley B.A., "Treatment of advanced head and neck cancer: What lessons have we learned?", in *J Clin Oncol*, v. 24, pp. 10231025, 2006.

[3] Datta N.R. et al., "Local hyperthermia combined with radiotherapy and-/or chemotherapy: Recent advances and promises for the future", in *Cancer Treatment Reviews*, v. 41, n. 9, pp. 742753, 2015.

[4] Hurwitz M., Stauffer P., "Hyperthermia, radiation and chemotherapy: the role of heat in multidisciplinary cancer care", in *Semin Oncol*, v. 41, pp. 714729, 2014.

[5] Horsman M.R., Overgaard J., "Hyperthermia: a potent enhancer of radiotherapy", in *Clin Oncol (R Coll Radiol)*, v. 19, pp. 418426, 2007.

[6] Gaffoglio R., *Hyperthermia Treatment Planning: a state-of-the-art overview*, Polytechnic University of Torino, I-10129 Torino, Italy.

[7] Paulides M.M., Dobsicek Trefna H., Curto S., Rodrigues D.B., "Recent technological advancements in radiofrequency- and microwave-mediated hyperthermia for enhancing drug delivery", in *Advanced Drug Delivery Reviews*, v. 163164, pp. 318, 2020.

[8] Hurwitz M., Stauffer P., "Hyperthermia, Radiation and Chemotherapy: The Role of Heat in Multidisciplinary Cancer Care", in *Seminars in Oncology*, v. 41, n. 6, pp. 714729, 2014.

[9] Horsman M.R., Overgaard J., "Hyperthermia: a Potent Enhancer of Radiotherapy", in *Clinical Oncology*, v. 19, n. 6, pp. 418426, 2007.

[10] Datta N.R. et al., "Local hyperthermia combined with radiotherapy and-/or chemotherapy: Recent advances and promises for the future", in *Cancer Treatment Reviews*, v. 41, n. 9, pp. 742753, 2015.

[11] van Rhoon G.C., *Hyperthermia: biology, clinical results and technology*, presentation, Erasmus MC Cancer Institute, Rotterdam.

[12] Paulides M.M., Dobsicek Trefna H., Curto S., Rodrigues D.B., "Recent technological advancements in radiofrequency- and microwave-mediated hyperthermia for enhancing drug delivery", in *Advanced Drug Delivery Reviews*, v. 163164, pp. 318, 2020.

[13] Vecchi G., "Energy in the electromagnetic field", Lecture in course *Applicazioni biomedicali dei campi elettromagnetici*, Antenna and EMC Lab, Politecnico di Torino, p. 1.

[14] Vecchi G., "The Bio-Heat Equation", Lecture in course *Applicazioni biomedicali dei campi elettromagnetici*, Antenna and EMC Lab, Politecnico di Torino, p. 7.

[15] Pennes H.H., "Analysis of tissue and arterial blood temperatures in the resting human forearm", in *J. Appl. Physiol.*, v. 1, pp. 93122, 1948.

[16] Kok H.P., van den Berg C.A., Bel A., Crezee J., "Fast thermal simulations and temperature optimization for hyperthermia treatment planning, including realistic 3D vessel networks", in *Med. Phys.*, v. 40, p. 103303, 2013.

[17] Paulides M.M., Sumser K., Ribeiro I.V.-B., Neufeld E., Van Rhoon G.C., "Challenges and opportunities in thermal tissue modelling for electromagnetic applications", in *2019 13th European Conference on Antennas and Propagation (EuCAP)*, Krakow, Poland, pp. 14, 2019.

[18] Gabriel S., Lau R.W., Gabriel C., "The dielectric properties of biological tissues: III. Parametric models for the dielectric spectrum of tissues", in *Phys. Med. Biol.*, v. 41, pp. 22712293, 1996.

[19] *ITIS Tissue Properties Database*, available at: https://itis.swiss/virtual-population/tissue-properties/overview/.

[20] La Gioia A., Porter E., Merunka I., Shahzad A., Salahuddin S., Jones M., OHalloran M., "Open-Ended Coaxial Probe Technique for Dielectric Measurement of Biological Tissues: Challenges and Common Practices", in *Diagnostics*, v. 8, n. 2, p. 40, 2018.

[21] Van de Kamer J.B., Van Wieringen N., De Leeuw A.A.C., Lagendijk J.J.W., "The significance of accurate dielectric tissue data for hyperthermia treatment planning", in *Int. J. Hyperthermia*, v. 17, pp. 123142, 2001.

[22] Rijnen Z., Bakker J.F., Canters R.A.M., Togni P., Verduijn G.M., Levendag P.C., Van Rhoon G.C., Paulides M.M., "Clinical integration of software tool VEDO for adaptive and quantitative application of phased array hyperthermia in the head and neck", in *International Journal of Hyperthermia*, v. 29, n. 3, pp. 181193, 2013.

[23] Paulides M.M., Stauffer P.R., Neufeld E., Maccarini P.F., Kyriakou A., Canters R.A.M., Van Rhoon G.C., "Simulation techniques in hyperthermia treatment planning", in *International Journal of Hyperthermia*, v. 29, n. 4, pp. 346357, 2013.

[24] Kok H.P., Wust P., Stauffer P.R., Bardati F., Van Rhoon G.C., Crezee J., "Current state of the art of regional hyperthermia treatment planning: a review", in *Radiation Oncology*, v. 10, p. 196, 2015.

[25] Paulides M.M. *et al.*, "Hyperthermia treatment planning and optimization", in *Physics in Medicine and Biology*, v. 55, p. 2465, 2010.

[26] Ishihara Y., Calderon A., Watanabe H., Okamoto K., Suzuki Y., Kuroda K., Suzuki Y., "A precise and fast temperature mapping using water proton chemical shift", in *Magnetic Resonance in Medicine*, v. 34, pp. 814823, 1995.

[27] Ludemann L., Wust P., Gellermann J., "Perfusion measurement using DCE-MRI: implications for hyperthermia", in *International Journal of Hyperthermia*, v. 24, pp. 9196, Feb. 2008.

[28] Kohler T., Maass P., Wust P., Seebass M., "A fast algorithm to find optimal controls of multiantenna applicators in regional hyperthermia", in *Physics in Medicine and Biology*, v. 46, pp. 25032514, 2001.

[29] Canters R.A.M., Franckena M., Paulides M.M., Van Rhoon G.C., "Patient positioning in deep hyperthermia: Influences of inaccuracies, signal correction possibilities and optimization potential", in *Physics in Medicine and Biology*, v. 54, pp. 39233936, 2009.

[30] Lagendijk J.J., Van Rhoon G.C., Hornsleth S.N., Wust P., De Leeuw A.C., Schneider C.J., Van Dijk J.D., Van Der Zee J., Van Heek-Romanowski R., Rahman S.A., Gromoll C., "ESHO quality assurance guidelines for regional hyperthermia", in *International Journal of Hyperthermia*, v. 14, n. 2, pp. 125133,

Mar.Apr. 1998

[31] Moler C., *Magic reconstruction for compressed sensing*, available at: Magic reconstruction for compressed sensing, accessed on February 7, 2025.

[32] Verhaart R.F. et al., "Accurate 3D temperature dosimetry during hyperthermia therapy by combining invasive measurements and patient-specific simulations", in *International Journal of Hyperthermia*, v. 31, pp. 686692, 2015.

[33] Groen et al., "Quantification of tissue property and perfusion uncertainties in hyperthermia treatment planning: Multianalysis using polynomial chaos expansion", in *Computer Methods and Programs in Biomedicine*, v. 240, 2023

[34] Di Donato L., Morabito A.F., *Microwave Imaging and Electromagnetic Inverse Scattering Problems*, available at: MDPI Journal of Imaging, accessed on December 1, 2024.

[35] Li H.-J., Kiang Y.-W., *The Electrical Engineering Handbook*, Elsevier Academic Press, 2004, pp. 686687.

[36] Rao S.M., *Time Domain Electromagnetics*, Ch. 7, pp. 243244, Auburn, AL, 1999.

[37] IEEE, *IEEE Standard Definitions of Terms for Antennas*, IEEE Std 145-1993.

[38] Bruggmoser G., Bauchowitz S., Canters R., Crezee H., Ehmann M., Gellermann J., Van Rhoon G., "Quality assurance for clinical studies in regional deep hyperthermia", in *Strahlentherapie und Onkologie*, v. 187, n. 10, p. 605, 2011.

[39] Sinesi M., *Minimally-invasive Temperature Monitoring in Hyperthermia Treatment of Internal Tumors via Detailed Numerical Phantoms*, Masters thesis, Politecnico di Torino, p. 58.

[40] ZMT Zurich MedTech AG, *Zurich Med Tech Sim4Life*, version 7.0.2, 2022, available at: https://zmt.swiss/sim4life/.

[41] Courant R., Friedrichs K., Lewy H., "On the partial difference equations of mathematical physics", in *IBM Journal of Research and Development*, v. 11, n. 2, pp. 215234, March 1967 [originally published in 1928].